Reconstructing Seawater $\delta^{18}O$ and $\Delta'^{17}O$ Values with Solid Earth System Evolution

Meng Guo[1*], Jordan A.G. Wostbrock[1], Noah J. Planavsky[1], Jun Korenaga[1],

[1]Department of Earth and Planetary Sciences, Yale University, New Haven, CT, USA.

*Correspondence: meng.guo@yale.edu

Highlights

- A new oxygen cycle model is built to systematically constrain the rates of low-temperature and high-temperature alteration using the evolution of continental crust and the thermal evolution of Earth.
- The reconstructed evolution of seawater $\delta^{18}O$ increased from a possible minimum of -10 to -5‰ at the late Archean to its present-day value, whereas the $\Delta'^{17}O$ value decreased from 0.015‰ $\pm$ 0.01‰ at the late Archean to ~0‰ modern.
- The evolution of seawater $\delta^{18}O$ requires rapid continental extraction in the early Earth.

Abstract

There has been extensive debate about how to link sedimentary oxygen isotope records to changes in solid Earth and surface processes. We present a new model of coupled ocean-crust-mantle evolution to investigate the geological processes that are responsible for the evolution of seawater $\delta^{18}O$ values. In our model, the rates of low- and high-temperature crustal alteration are constrained by mantle cooling and crustal evolution. This way, we were able to outline the possible path of solid Earth evolution that matches the observed seawater $\delta^{18}O$ records. Our results suggest that marine $\delta^{18}O$ values may have been as low as -10‰ to -5‰ in the late Archean. The corresponding $\Delta'^{17}O$ value may have been 0.015‰ $\pm$ 0.01‰ in the late Archean and then decreased with time. The evolution of seawater $\delta^{18}O$ is shown to be sufficiently sensitive to the history of continental formation, and our modeling suggests the presence of a considerable amount of continental crust in the early Archean.

Keywords

Seawater $\delta^{18}O$ and $\Delta'^{17}O$, crustal growth, solid Earth system evolution

1. Introduction

The significance of sedimentary oxygen isotope records has been debated for decades. A well-established secular increase in $\delta^{18}O$ values ($\delta^{x}O$ (‰) = 1000 · (R^{x}_{sample} /R^{x}_{SMOW} - 1) and R^{x}_{sample} is the $^{x}O/^{16}O$ ratio of the sample, where x is 17 or 18) is observed in sedimentary records, where the $\delta^{18}O$ values of Archean sediments are ~10‰ to 20‰ lower than that of modern (e.g., Knauth and Epstein, 1976; Galili et al., 2019). From Archean to Phanerozoic, the $\delta^{18}O$ values of chert increased from ~15‰ to ~30‰ (e.g., Robert and Chaussidon, 2006; Bindeman et al., 2016 and references therein), shale increased from ~10‰ to ~15‰ (e.g., Bindeman et al., 2016 and references therein), and marine carbonate increased from ~-13‰ (relative to PDB) to a maximum of 0‰ (e.g., Prokoph et al., 2008 and references therein). Recently, high-precision paired $\delta^{17}O$-$\delta^{18}O$ measurements (hereafter referred to as $\Delta'^{17}O$ where $\Delta'^{17}O = 1000 \cdot (\ln(\delta^{17}O/1000 + 1) - 0.528 \cdot \ln(\delta^{18}O/1000 + 1)$; see Wostbrock and Sharp, 2021, for details) have been used to provide an additional constraint to interpret the observed $\delta^{18}O$ records. The $\Delta'^{17}O$ value of chert gradually decreases as the $\delta^{18}O$ value increases from ~3.5 Ga to present-day (e.g., Zahkarov et al., 2021; Sengupta et al., 2020; Liljestrand et al., 2020; Lowe et al., 2020; Levin et al., 2014).

Two end-member explanations have been proposed to explain this global sedimentary trend. The first hypothesis suggests that the early ocean was significantly hotter (>70°C) than the present (e.g., Knauth and Epstein, 1976; Robert and Chaussidon, 2006), and that the $\delta^{18}O$ of seawater has remained relatively constant through time. An alternative hypothesis is that the temperature of the surface ocean has remained relatively constant over time, requiring the $\delta^{18}O$ value of seawater to increase by ~10‰ in sync with the sedimentary $\delta^{18}O$ record (e.g., Walker and Lohmann, 1989; Jaffrés et al., 2007). Recently, Galili et al. (2019) utilized marine iron oxides, whose $\delta^{18}O$ has only a weak temperature-dependence (~1‰ per 20℃), to support the second hypothesis. According to Galili et al. (2019), there was a shift in seawater $\delta^{18}O$ from -8‰ at 2 Ga to 0‰ in the early Phanerozoic. However, the history of seawater $\delta^{18}O$ is still highly debated.

Suggested Archean seawater $\delta^{18}O$ values range from -13.3‰ to +3.3% (e.g., Muehlenbachs et al., 2003; Jaffrés et al., 2007; Johnson and Wing, 2020). For example, modeling of the geological water cycle suggests that seawater $\delta^{18}O$ may have been as low as -13.3‰ at ~3.4 Ga and gradually increased to -0.3‰ at present-day (Jaffrés et al., 2007). Jaffrés et al. (2007) explains this increasing trend with two stepwise increases in the ratio of high- to low-temperature water/rock interactions

over geological history. On the other hand, studies using ophiolites of altered oceanic crust indicate that seawater $\delta^{18}O$ is likely to be buffered at 0‰ in the past (e.g., Muehlenbachs, 1998; Muehlenbachs et al., 2003). This buffering effect would be achieved through a constant ratio of high-to-low temperature alteration. More recently, studies on Archean altered oceanic crust suggested that the ocean $\delta^{18}O$ value would have been higher in the past and decreased over time. Pope et al. (2012) studied Isua Supracrust Belt serpentines to suggest that the $\delta^{18}O$ value of the Eoarchean ocean was between +0.8 and +3.8‰. Johnson and Wing (2020) examined ~3.24-billion-year-old hydrothermally altered oceanic crust from the Panorama district in the Pilbara Craton and suggested that the ocean had an $\delta^{18}O$ value of $+3.3 \pm 0.1$‰. Using a water cycle model, they explain the decreasing ocean $\delta^{18}O$ record with the emergence of continental crust (increasing the low-temperature alteration flux) after the late Archean.

Previous studies do not include comprehensive modeling of solid Earth and the role it may have on marine chemical evolution. The oxygen isotopic composition of seawater is controlled primarily by hydrothermal alteration of oceanic crust, continental weathering, and subduction of water and crustal materials (e.g., Muelenbachs, 1998; Wallmann, 2001). Larger fractionation values occur during low-temperature alteration processes, where the heavier isotopes, ^{18}O and ^{17}O, are preferentially incorporated into secondary minerals. This results in lower $\delta^{18}O$ and $\delta^{17}O$ values of seawater relative to modern. Smaller fractionation values occur during high-temperature alteration, increasing the $\delta^{18}O$ and $\delta^{17}O$ values of seawater relative to modern. The evolution of the solid Earth system has major control over the history of oxygen fractionation in seawater. The secular cooling of the mantle controls the rates of hydrothermal alteration and subduction of crust, whereas the history of crustal formation is directly linked to the rate of continental weathering. Therefore, it is desirable to interpret geochemical records with a theoretical framework that is consistent with the solid Earth system evolution (e.g., Korenaga et al., 2017; Guo and Korenaga, 2020). In this regard, developing a quantitative model of coupled ocean-crust-mantle evolution is essential for interpreting the seawater oxygen isotope evolution.

Here we present a comprehensive model of solid Earth evolution coupled to a mass balance model of seawater oxygen isotope ratios to investigate the geological processes that are responsible for the evolution of seawater $\delta^{18}O$ and $\Delta'^{17}O$ values. This is the first model to systematically constrain the changing proportion of high-temperature versus low-temperature crustal alteration using the history of mantle cooling and crustal formation. To achieve this, we make use of the

distributions of continental formation age (Korenaga, 2018) and surface age (Roberts and Spencer, 2015) to constrain the extent of crustal recycling and reworking as well as the Archean and Proterozoic mantle potential temperatures (Herzberg et al., 2010) to constrain the thermal history of Earth. We compared and examined the three end-number seawater $\delta^{18}O$ values in the Archean, -13.3‰ (Jaffrés et al., 2007), 0‰ (e.g., Muehlenbachs et al., 2003), and +3.3‰ (Johnson and Wing, 2020), and the evolution of seawater $\delta^{18}O$ in the Phanerozoic and Proterozoic is constrained by iron oxides records (Galili et al., 2019 and references therein). The calculated seawater $\delta^{18}O$ and $\Delta'^{17}O$ evolutions are compared with the observed sedimentary records (Zahkarov et al., 2021; Sengupta et al., 2020; Liljestrand et al., 2020; Bindeman et al., 2016; Prokoph et al., 2008; Levin et al., 2014; Lowe et al., 2020; and references therein). As a result, we improve the previous simulation scheme of seawater $\delta^{18}O$ by grounding the alteration rates with geophysical constraints and provide a first-order estimate on the seawater $\Delta'^{17}O$ evolution.

2. Methods

Our box model of seawater $\delta^{18}O$ and $\Delta'^{17}O$ tracks the compositional evolution of six terrestrial reservoirs: mantle, seawater, marine sediments, high- and low-temperature altered oceanic crusts, and continental crust. Wallmann (2001) built a comprehensive model for seawater $\delta^{18}O$ during the Phanerozoic, and the overall setup of our model draws upon many aspects of his model. However, we modified the model to track the evolution of seawater $\delta^{18}O$ and $\Delta'^{17}O$ through Earth history in a self-consistent fashion.

In our model, the quantitative constraints on hydrothermal alteration rates are directly linked to constraints on solid Earth evolution (following Guo and Korenaga, 2020), which determine the seawater ^{18}O fluxes. For $\Delta'^{17}O$ evolution of seawater, we relate the high and low-temperature fluxes to a θ value, which is a variable relating the $\delta^{18}O$ and $\delta^{17}O$ fractionation between two phases and varies with temperature during equilibrium processes (Cao and Liu, 2011). Our model also includes changing ocean mass and the effect of crustal reverse weathering. Reverse weathering describes the in situ authigenesis of non-kaolinite-type (cation-poor) phyllosilicate minerals (clays) (e.g., Isson and Planavsky, 2018). In this section, we first explain the overall model setup of seawater $\delta^{18}O$ and $\Delta'^{17}O$ values. We then describe the constraints of crustal formation and thermal evolution history on the rates of high- and low-temperature alteration rates.

2.1 The seawater $\delta^{18}O$ and $\Delta'^{17}O$ model

The exchange of oxygen between seawater, mantle, and crust is controlled by temperature. In our model, high-temperature alteration (>150°C) includes on-axis hydrothermal alteration, serpentinization, and alteration at hydrothermal vents, whereas low- to mid-temperature alterations (<150°C) include off-axis hydrothermal alteration such as Urey reactions and reverse weathering.

To track the evolution of seawater $\delta^{18}O$, we consider the evolution of the total abundance of oxygen as well as its isotopic composition in seawater through Earth history. Our strategy is to track the mass fluxes of oxygen between terrestrial reservoirs (Fig. 1) and then calculate the corresponding fluxes of ^{18}O (Fig. 2). The exchange of oxygen among different reservoirs is mainly controlled by the creation and subduction of crustal materials and their hydrothermal alteration. Through magmatism, oxygen can be fixated in the crust (F_{mHT}, F_{mLT}, and F_{mw}) at mid-ocean ridges, hotspot islands, and back-arc basins. After formation, oceanic crust can exchange oxygen with seawater through weathering (F_w), reverse weathering (F_{rev}), and high- and low-temperature crustal alteration (F_{HT} and F_{LT}). During subduction, oxygen can be released from downgoing slabs due to the breakdown of hydrated minerals under high temperatures and pressures, and the released volatiles can be degassed through arc and back-arc magmatism and eventually end up in seawater (F_{reHT}, F_{reLT}, and F_{rew}). The rest of the oxygen in the slab is then recycled into the mantle at subduction zones as chemically bound water and pore water (F_{sHT}, F_{sLT}, and F_{sw}). The proportion of the released oxygen to the total oxygen content in the subducting slab is characterized by recycling rates (r_{HT}, r_{LT}, and r_w).

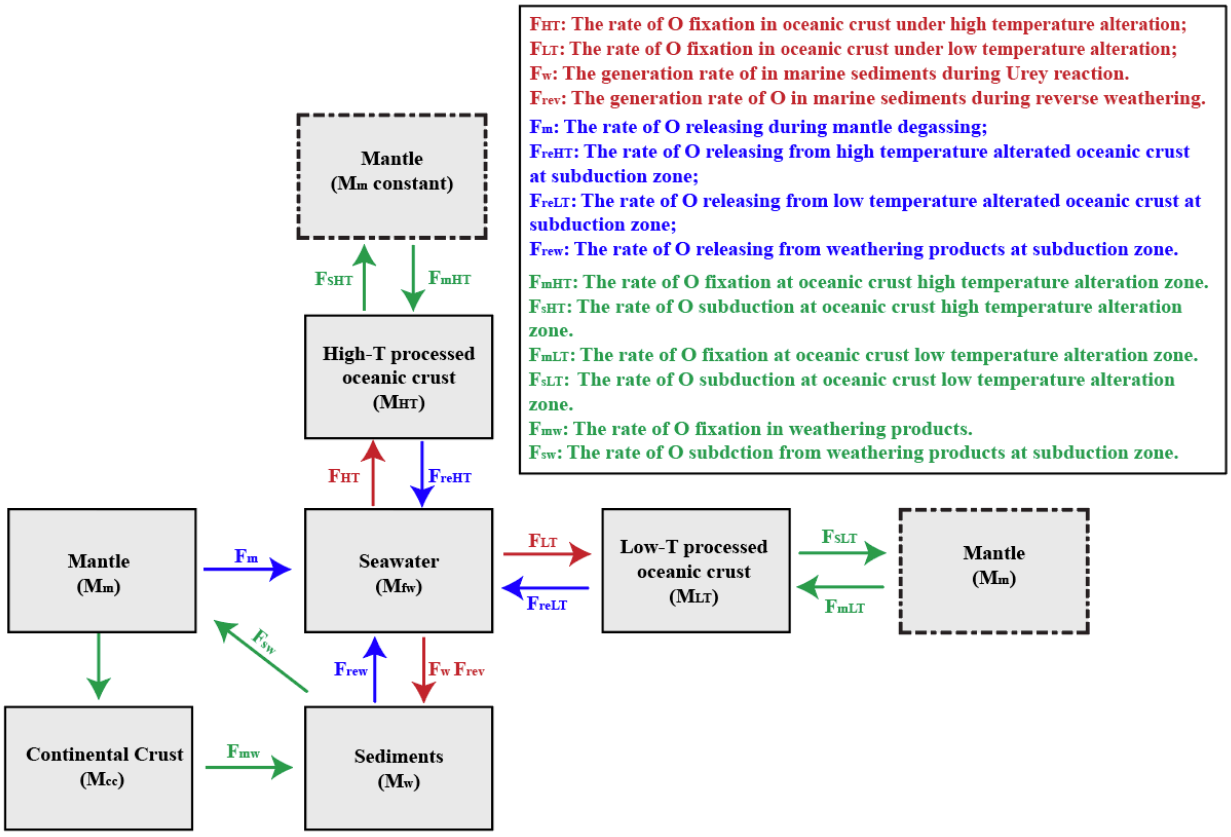

Fig. 1. Model structure of oxygen fluxes between terrestrial reservoirs. The blue and red arrows represent the oxygen fluxes that are transferred from crust and mantle into seawater and vice versa, respectively. The green arrows represent the oxygen fluxes that are exchanged between crust and mantle. The dashed box labeled "Mantle" is the same reservoir as the solid one.

Based on the oxygen fluxes between terrestrial reservoirs, we track the exchange of ^{18}O by considering both their transfer along with the total mass fluxes as well as their exchange between seawater, oceanic crust, and weathering products during alternation (Fig. 2). The major mass balance relationships considered in this model are listed in Table S1. The amount of ^{18}O transferred along with the water fluxes are calculated based on their isotope fraction during oxygen fixation under different temperatures (Table S2). The rate of ^{18}O exchanged between terrestrial reservoirs is controlled by the history of mantle cooling and crustal alteration. In our model, the rate of high-temperature alteration of oceanic crust (f_{HT}) is constrained by the thermal evolution of the mantle, whereas the rate of low-temperature alteration (f_{LT}) is inferred from the mass balance of surface volatiles. The non-dimensional variables, f_{HT} and f_{LT}, represent the relative changes in high- and low-temperature alteration activities with respect to their present-day values. The present-day mass

transfer rates are estimated based on relevant geological and geochemical observations (Table S3). On the other hand, oxygen isotope exchange between seawater and crust, which proceed by dissolution and precipitation of minerals as well as isotope diffusion, are modeled by means of isotopic saturation indices (Ω, Table S2 and S3).

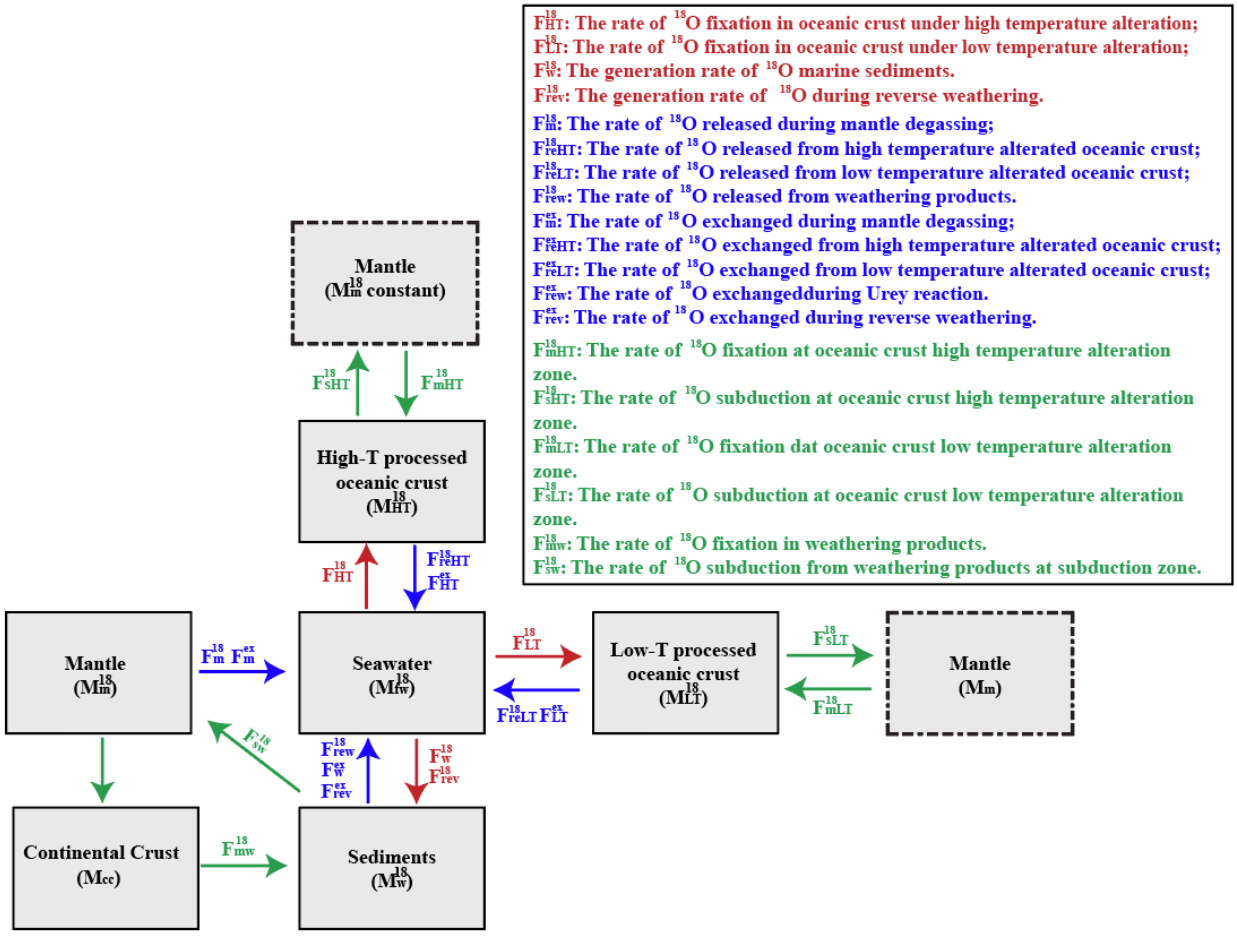

Fig. 2. Model structure of ^{18}O fluxes between terrestrial reservoirs. The blue and red arrows represent the ^{18}O fluxes that are transferred from crust and mantle into seawater and vice versa, respectively. The green arrows represent the ^{18}O fluxes that are exchanged between crust and mantle. The dashed box labeled "Mantle" is the same reservoir as the solid one.

We calculate the seawater Δ'^{17}O based on the modeled δ^{18}O value and the relative proportions of high-, mid-, and low-temperature fluxes. First, as ^{17}O follows the same fractionation processes with ^{18}O but with different magnitude, the seawater δ'^{17}O value can be calculated through time according to δ'^{18}O:

$$\delta'^{17}\mathrm{O} = \lambda_{\mathrm{seawater}}\, \delta'^{18}\mathrm{O}, \quad (1)$$

where $\delta'^{X}O = 1000*\ln(\delta^{X}O/1000+1)$ and x is either mass 17 or 18, and $\lambda_{seawater}$ is calculated based on an assigned θ value for each temperature flux and the relative proportion of each flux at each timestep as follows. The variable θ relates the $\delta^{18}O$ and $\delta^{17}O$ fractionation between two phases and varies with temperature during equilibrium processes (Cao and Liu, 2011). Knowing that θ values change between ~0.524 at low temperature to 0.5305 at high temperature, we assign each flux a different θ value according to temperature (low-T = 0.524-0.525; mid-T = 0.525-0.526, and high-T = 0.527-0.528; Table S4). This range in θ values is reasonable based on the θ-T relationship of silicates and water (e.g., Wostbrock and Sharp, 2021 and references therein). The percent of each temperature flux is tracked through time by adding each temperature flux and dividing by the total flux. We then multiply each θ with its corresponding flux percent and add the three variables together to construct a $\lambda_{seawater}$ value. Lastly, the seawater $\Delta'^{17}O$ is calculated as (see Wostbrock and Sharp, 2021 for more details):

$$\Delta'^{17}O = \delta'^{17}O - 0.528\ \delta'^{18}O. \quad (2)$$

2.2 Constraining the rate of high-temperature alteration (f_{HT}) using the thermal evolution of mantle

The high-temperature alteration factor f_{HT} is controlled by the processing rate of mantle at mid-ocean ridges and arc systems, which is closely related to plate velocity. Thus, the non-dimensional variable f_{HT} is set to be proportional to plate velocity as:

$$f_{HT}(t) = \left(\frac{V(t)}{V(t_p)}\right)^n, \quad (3)$$

where t is time, t_p refers to the present day, and n is a constant, whose value can vary between 1 and 3. When n equals 1, this formulation corresponds to a linear dependence of high-temperature alteration of oceanic crust on plate velocity (e.g., Wallmann, 2001), whereas n greater than 1 represents a nonlinear dependence. The possibility of a nonlinear relationship is suggested from several observations. First, the number density of hydrothermal vents is roughly linearly proportional to spreading rate (Baker and German, 2004), but the activity level of hydrothermal vents is very sensitive to the depth of axial magma chamber at the mid-ocean ridges, with shallow magma chambers allowing greater vent activities (Baker, 2009). Second, the depth of the axial magma chamber is a strongly nonlinear function of spreading rate (e.g., Phipps Morgan and Chen, 1993). The oxygen isotope composition of hydrothermal vent fluids suggests that the extent of

high-temperature water-rock reaction is greater at hydrothermal vents on a slower spreading ridge (Bach and Humphris, 1999); however, this effect is not strong enough to cancel the above sources of nonlinearity. Slower plate velocity in the past is accompanied by higher mantle potential temperature and greater magma supply (Korenaga, 2006, 2018), but the effect of mantle potential temperature is likely to be weaker compared to the effect of spreading rate (Chen, 2004). In fact, hydrothermal vent activity is virtually absent along the slow-spreading Reykjanes Ridge (German and Parson, 1998), which is located adjacent to the Iceland hotspot. Even though the details of high-temperature water-rock reaction at the global mid-ocean ridge system are yet to be understood, therefore, one cannot overlook the possible nonlinear dependence of high-temperature hydrothermal processes on plate velocity. We thus test values from 1 to 3 for the exponent n in equation (3).

To track the high-temperature alteration factor f_{HT}, we need to know the temporal evolution of plate velocity $V(t)$. By utilizing its relationship with surface heat flux, $V(t)$ can be expressed as (Korenaga, 2006):

$$V(t) = V(t_p) \left(\frac{Q(t)}{Q(t_p)} \frac{T_p(t_p)}{T_p(t)} \right)^2, \quad (4)$$

where the present-day plate velocity $V(t_p)$ is 5 cm/yr (Parsons, 1981), the present-day mantle potential temperature $T_p(t_p)$ is 1350 ℃ (Herzberg et al., 2010), and the present-day mantle heat flux $Q(t_p)$ is calculated as the difference between the total surface heat flux (46 ± 3 TW; Jaupart et al., 2007) and the heat production of continental crust (7.5 ± 2.5 TW; Rudnick and Gao, 2003). To solve equation (4), all we need is the history of mantle potential temperature $T_p(t)$ and mantle heat flux $Q(t)$.

Using the global energy balance (Korenaga, 2017), the mantle potential temperature $T_p(t)$ is calculated backward in time as:

$$C_m \frac{dT_p(t)}{dt} = H(t) - Q(t) + Q_c(t), \quad (5)$$

where C_m is the heat capacity of the whole mantle (4.97×10^{27} J/K), H *is* the mantle heat production, Q is the mantle heat flux, and Q_c is the core heat flux.

To solve equation (5), first, the mantle heat production H is tracked backward in time with the heat production rates and decay constants of heat producing elements (^{238}U, ^{235}U, ^{232}Th, and ^{40}K) within the mantle (Korenaga, 2006). Second, the mantle heat flux Q is assumed to be constant at

~36 TW throughout the entire Earth history following Korenaga (2017). Finally, the core heat flux Q_c is considered to be linearly decreasing through time, with the difference between initial and present-day core heat flux (ΔQ_c) varying between 2 to 5 TW (O'Rourke et al., 2017). The present-day core heat flux is set to be a free parameter varying between 5 to 15 TW (O'Rourke et al., 2017). The parameters used in the thermal evolution model are listed in Table S5. To summarize, the mantle potential temperature can be obtained by integrating equation (5) backward in time with H, Q, and Q_c, which is checked against observations (Herzberg et al., 2010). The evolution of plate velocity can then be tracked with equation (4), and the high-temperature alteration factor f_{HT} can be calculated from plate velocity using equation (3).

2.3 Constraining the rate of low-temperature alteration (f_{LT}) using the thermal evolution of mantle and the history of continental formation

We constrain the factor of low-temperature alteration f_{LT} by utilizing the surface mass balance of carbon dioxide (CO_2). During mantle magmatism and continental recycling and weathering, volatiles like CO_2 are released into the atmosphere and eventually end up in oceans. Because CO_2 is an important greenhouse gas, it has to be consumed during low-temperature alteration of oceanic crust and continental weathering (e.g., Coogan and Gillis, 2020), to obtain a relatively constant global temperature (e.g., Galili et al., 2019). Thus, using both the history of crustal growth and the thermal evolution of Earth, f_{LT} may be calculated as follows:

$$f_{LT}(t) = \frac{K_{mo}(t) + K_{mp}(t) + K_{mc}(t) + f_{CC/M}K_{rc}(t) + f_{CC/M}K_{rw}(t)}{K_{mo}(t_p) + K_{mp}(t_p) + K_{mc}(t_p) + f_{CC/M}K_{rc}(t_p) + f_{CC/M}K_{rw}(t_p)}, \quad (6)$$

where K_{mo}, K_{mp}, and K_{mc} are the mantle processing rates during the generation of oceanic crust, hotspot islands, and continental crust, respectively; K_{rc} and K_{rw} are the rates of continental recycling and reworking, respectively; and $f_{CC/M}$ is the ratio of the carbon dioxide released from the same amount of continental crust and mantle during geological processes. In our model, the term "crustal recycling" denotes the loss of continental crust to the mantle through subduction and delamination, whereas "crustal reworking" indicates the processes that change isotopic compositions and reset the apparent age of the established crust (e.g., erosion, weathering, and intra-crust partial melting). Recent studies of global carbon flux suggest that mid-ocean ridges and subducting sediments emit CO_2 at similar rates of ~20 Mt C yr^{-1} (e.g., Plank and Manning, 2019), and because the mantle processing rate beneath mid-ocean ridges and the recycling rate of

continental crust are ~0.69 x 10^{24} kg Gyr^{-1} (Korenaga, 2006) and ~0.7-0.9 x 10^{22} kg Gyr^{-1} (e.g., Stern and Scholl, 2010), respectively, we consider $f_{CC/M}$ to be ~100 in our model.

To calculate f_{LT} using equation (6), K_{mo}, K_{mp}, K_{mc}, K_{rc}, and K_{rw} need to be constrained. Among these, K_{mo} and K_{mp} can be inferred from the thermal evolution of the mantle, whereas K_{mc}, K_{rc}, and K_{rw} can be obtained from a model of continental growth. First, considering that volcanism at mid-ocean ridges is due to decompressional melting, K_{mo} is directly linked with the initial depth of mantle melting Z and plate velocity V:

$$K_{mo}(t) = K_{mo}(t_p)\frac{Z(t)\,V(t)}{Z(t_p)V(t_p)}, \quad (7)$$

where $K_{mo}(t_p)$ is the present-day rate of oceanic crust generation, which is considered to be 6.7x10^{14} kg/yr (Korenaga, 2006). The evolution of plate velocity $V(t)$ is obtained in the thermal evolution model as described in section 2.2. The initial depth of melting Z is controlled by mantle potential temperature T_p:

$$Z(t) = \frac{T_p(t) - 1150}{g\rho_m(1.2 \text{ x } 10^{-7} - (dT/dP)_S)}, \quad (8)$$

where g is gravitational acceleration (9.8 m/s^2), ρ_m is mantle density (3300 kg/m^3), $(dT/dP)_S$ is the adiabatic gradient in the mantle (1.54 x 10^{-8} K/Pa), the evolution of mantle potential temperature $T_p(t)$ is obtained in the thermal evolution model (section 2.2), 1150 ℃ is the surface temperature of the mantle solidus, and 1.2 x 10^{-7} K/Pa is the gradient of mantle solidus.

Second, we assume a linear relation between the rate of mantle magmatism at hotspot islands K_{mp} and core heat flux Q_c:

$$K_{mp}(t) = K_{mp}(t_p)\frac{Q_c(t)}{Q_c(t_p)}, \quad (9)$$

where $K_{mp}(t_p)$ is the plume mass flux at present, which can be estimated from the present-day plume buoyancy flux, and the evolution of core heat flux is calculated in section 2.2.

Third, we solve for the crustal recycling rate (K_{rc}) using the history of crustal formation. Following Rosas and Korenaga (2018), the rates of crustal generation K_{cc} and recycling K_{rc} are parameterized as follows:

$$M_{cc}(t) = \frac{M_{cc}(t_p)}{1-e^{-\kappa g(t_p-t_s)}}\left(1 - e^{-\kappa g(t-t_s)}\right), \quad (10)$$

$$K_{rc}(t) = R_s + \frac{R_p-R_s}{1-e^{-\kappa r(t_p-t_s)}}\left(1 - e^{-\kappa r(t-t_s)}\right), \quad (11)$$

$$\frac{dM_{cc}(t)}{dt} = K_{cc}(t) - K_{rc}(t), \quad (12)$$

where $M_{cc}(t)$ is continental mass at time t, $M_{cc}(t_p)$ is the present-day crustal mass (2.09 x10^{22} kg), K_{cc} is the crustal generation rate, and K_{rc} *is* the crustal recycling rate. In equations (10) and (11), the term t_s denotes the onset of crustal formation; κ_g and κ_r are the decay constants for K_{cc} and K_{rc}, respectively; and R_s and R_p are the rates of crustal recycling at t_s and t_p, respectively. In this parametrization, $M_{cc}(t)$ and $K_{rc}(t)$ are first calculated from the assumed values of these model parameters, and then equation (12) is used to calculate $K_{cc}(t)$. A wide range of crustal growth patterns can be simulated by varying these parameters, and different crustal growth models yield different evolutions of K_{rc} and K_{cc}.

Fourth, we infer the mantle processing rate during the generation of continental crust (K_{mc}) from the rate of crustal generation K_{cc}. As suggested by equation (12), the net growth rate of continental crust equals the difference between crustal generation rate K_{cc} and recycling rate K_{rc}. However, considering that the continental crust does not result from single-stage melting of the mantle, at least part of the crust is likely to be produced through the secondary melting of oceanic crust. Thus, to avoid overestimating the mantle processing rate during continental generation, the contribution of oceanic crust needs to be deducted from K_{cc} following Guo and Korenaga (2020) (see their equations (4) and (5)).

Lastly, we assume that the crustal reworking rate K_{rw} is proportional to crustal recycling, considering that reworking facilitates breaking down crustal rocks into smaller fragments, which are further subjected to subduction. Thus, the temporal evolution of reworking is assumed to be in sync with recycling but scaled by a factor of f_{rw}, which varies between 0.1 to 0.8. The crustal reworking rate can be expressed as:

$$K_{rw}(t) = f_{rw}K_{rc}(t). \quad (13)$$

The crustal recycling and reworking rates are checked against the crustal formation age distribution (Korenaga, 2018) and surface age distribution (Roberts and Spencer, 2015), following Guo and Korenaga (2020) (see their equations (7) to (11)). Note that crustal reworking constrained by these two age distributions is mostly about the partial melting of preexisting continental crust, so it serves as an additional source of atmospheric CO_2. The parameters used in the crustal evolution are listed in Table S5.

3. Results

We conduct our modeling in three stages using Monte Carlo sampling, in a manner similar to Guo and Korenaga (2020). First, we test a wide range of crustal evolution scenarios, where we assume substantial continental growth correlates to crustal mass emergence. We consider models that span from instant continental growth to late-stage growth. We only force the model with scenarios that satisfy previously proposed, empirically based distributions of crustal formation ages (Korenaga, 2018 and references therein) and surface ages (Roberts and Spencer, 2015) (Figs. 3A and 3B).

Next, we couple the selected crustal growth models from the first stage with different models of mantle thermal evolution, by considering the uncertainties of heat production and heat fluxes of terrestrial reservoirs. The appropriate combinations of crustal and thermal evolution are selected according to the history of mantle cooling during the Archean and Proterozoic (Herzberg et al., 2010) (Fig. 3C).

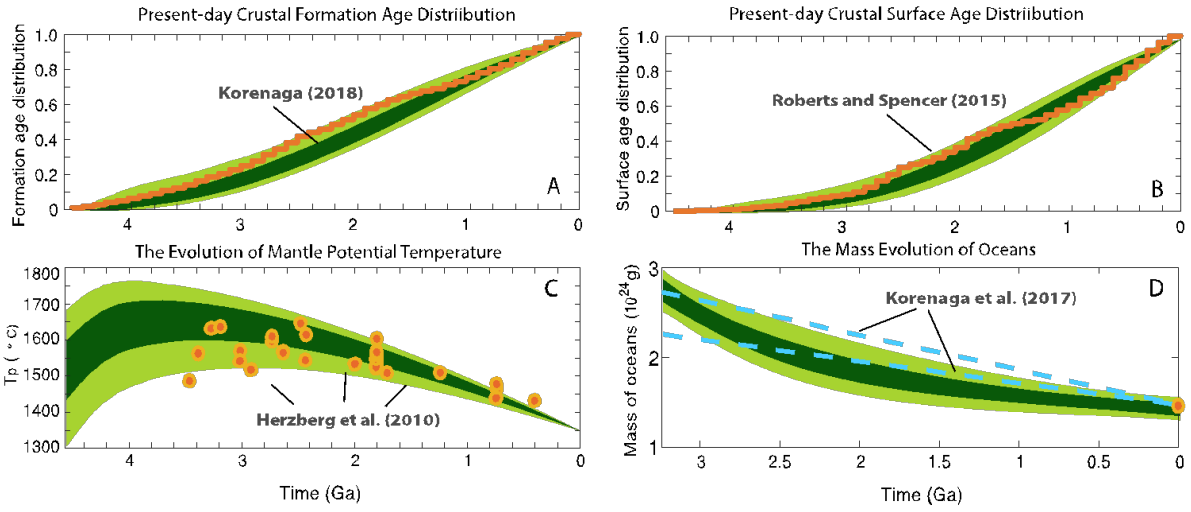

Fig. 3. Observational constraints and the distribution of successful model solutions. Observational constraints used to select successful solutions are shown in orange. The middle 50% and 90% of successful solutions are shown in dark green and light green, respectively. (A) Formation age distribution of continental crust (Korenaga, 2018), (B) surface age distribution of continental crust (Roberts and Spencer, 2015), (C) Mantle potential temperature (Herzberg et al., 2010), and (D) history of oceans mass. In (D), the history of ocean mass is compared with the freeboard-based estimate of Korenaga et al. (2017), which is shown in blue dashed lines. The freeboard-based estimate is shown only for comparison; it is not used to select successful solutions. (A-C) are modelled throughout the Earth's history, whereas (D) is modelled with the evolution of seawater $\delta^{18}O$ and $\Delta'^{17}O$, from 3.5 Ga to present day.

Lastly, we determine the rates of high- and low-temperature alteration of oceanic crust (f_{HT} and f_{LT}) using the accepted combinations of crustal and thermal evolutions and calculate the corresponding evolution of seawater $\delta^{18}O$ and $\Delta'^{17}O$. The evolution of ocean mass is also tracked in our model and is compared with the freeboard-based estimates (Korenaga et al. 2017) (Fig. 3D). In this stage of modeling, we test three scenarios of proposed marine $\delta^{18}O$ records, with the mid-Archean seawater $\delta^{18}O$ of +3.3‰ (Johnson and Wing, 2020), 0‰ (e.g., Muelenbachs, 1998; Muehlenbachs et al., 2003), and -13.3‰ (Jaffrés et al., 2007) (Figs. 4A-C). The successful results are selected according to the estimates of marine $\delta^{18}O$ from iron oxides in the Proterozoic and the Phanerozoic (Galili et al., 2019) and modern seawater $\delta^{18}O$ value (0 ± 2‰). The reconstructed seawater $\delta^{18}O$ evolution is also compared with the $\delta^{18}O$ trend recorded in carbonates (Prokoph et al., 2008 and references therein), chert (Zahkarov et al., 2021; Sengupta et al., 2020; Liljestrand et al., 2020; Bindeman et al., 2016; Levin et al., 2014; and references therein), and shale (Bindman et al., 2016 and references therein). The corresponding seawater $\Delta'^{17}O$ (Figs. 4D-F) are calculated and selected according to its modern value ($0‰ \pm 0.005\%$), whose evolution is compared with the chert records (Zahkarov et al., 2021; Sengupta et al., 2020; Liljestrand et al., 2020; Lowe et al., 2020; Levin et al., 2014; and references therein). It should be noted that the sedimentary records (except iron oxides) of $\delta^{18}O$ and $\Delta'^{17}O$ are shown only for comparison but not used to select successful solutions. The corresponding crustal evolutions from the successful solutions are shown in Figs. 4G-I.

As can be seen from the successful Monte Carlo solutions (Fig. 4), by solely varying the relative proportion of f_{HT} to f_{LT} according to the history of crustal evolution and the thermal evolution of the mantle, we are able to reproduce the inferred seawater $\delta^{18}O$ evolution, and the corresponding $\Delta'^{17}O$ agrees with the decreasing trend of chert without using such a constraint. The results suggest that seawater $\delta^{18}O$ may have changed substantially through time — increasing from a possible minimum of $-10‰ \pm 2‰$ at the end of Archean to modern value (Figs. 4A-C). Consequently, the corresponding evolution of $\Delta'^{17}O$ may be as high as $0.015‰ \pm 0.005‰$ at the end of Archean and then decreased with time. Results from Fig. 4 are based on the ^{18}O mole fraction of sedimentary rocks from Jaffres et al. (2007) and Wallmann (2001) ($\phi_{si} = 2.017 \times 10^{-3}$), see Table S4). Our model results are sensitive to ϕ_{si} values, which are not well-constrained through Earth history; therefore, we re-run the model with a ϕ_{si} consistent with modern day ^{18}O mole fraction of sedimentary rock

(ϕ_{si}= 2.037x10^{-3}). Results from the Monte Carlo show the same shape of the δ^{18}O value of seawater through time, though the minimum value is ~-5‰ $\pm$ 2‰ in the late Archean (Fig. S1). These results demonstrate that the proposed seawater δ^{18}O records can be reconstructed by using constraints from solid Earth evolution. Critically, all the successful evolutions of seawater δ^{18}O requires rapid continental growth in the early Earth (Figs. 4G-I), with the mass of continental crust reaching its present-day level by the end of the Hadean to early Archean. We collected a total number of ~3 x 10^3 successful solutions for each scenario of seawater δ^{18}O evolution. Our modeling scheme ensures that the final successful solutions satisfy the thermal evolution of mantle, the mass of present-day oceans, the distribution of crustal formation age and surface age within reasonable uncertainties (Fig. 3), and the present-day, the Proterozoic, and the Phanerozoic seawater δ^{18}O (Galili et al., 2019) (Fig. 4). The figures shown in the Results section are from successful solutions of the first scenario where the initial seawater δ^{18}O = +3.3‰ (except for Figs. 4 and 7 where all initial δ^{18}O seawater values are shown), because the model selected crustal and thermal evolution are very similar. All figures for all scenarios are provided in the supplementary information (Figs. S1-S6).

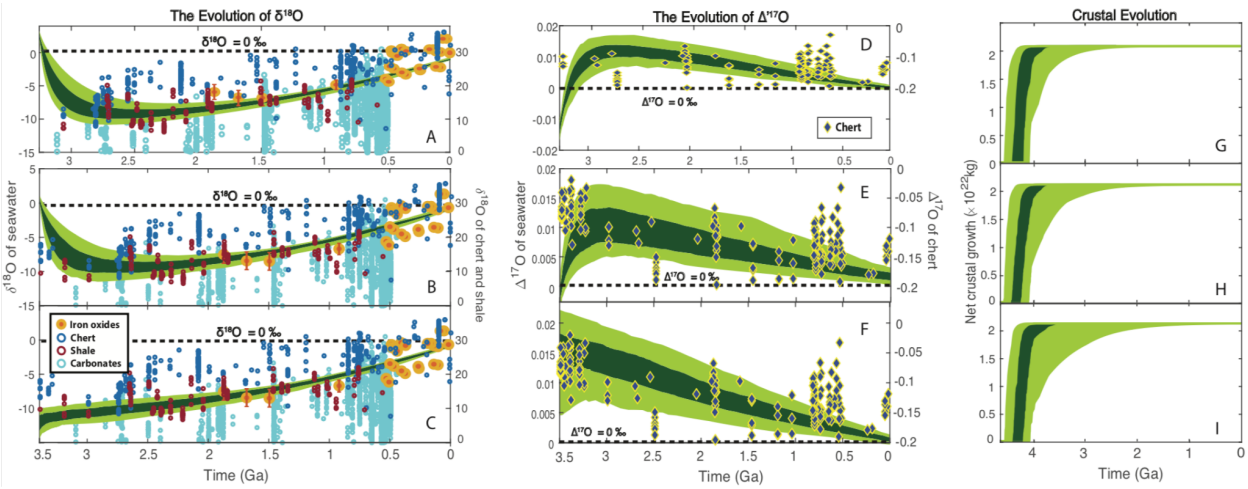

Fig. 4. The simulated Monte Carlo solutions of the seawater δ^{18}O and Δ'^{17}O evolutions with ϕ_{si}=2.017x10^{-3}. The evolution of seawater δ^{18}O and the corresponding Δ'^{17}O and crustal evolution for the initial conditions of (A, D, G) +3.3‰ (Johnson and Wing, 2020), (B, E, H) 0‰ (e.g., Muehlenbachs et al., 2003), and (C, F, I) -13.3‰ (Jaffrés et al., 2007), respectively. The middle 50% and 90% of successful solutions are shown in dark green and light green, respectively. The iron oxide records (Galili et al., 2019) are shown in orange circles; carbonates (Prokoph et al., 2008 and references therein) are shown in light blue circles; chert and shale (Zahkarov et al., 2021; Sengupta et al., 2020;

Liljestrand et al., 2020; Bindeman et al., 2016; Levin et al., 2014; and references therein) are shown in dark blue and red circles. The $\delta^{18}O$ of carbonates, chert, and shale are shown for comparison but not used to select successful solutions. The corresponding evolution of seawater $\Delta'^{17}O$ for (A) to (C) are compared with chert records (Zahkarov et al., 2021; Sengupta et al., 2020; Liljestrand et al., 2020; Lowe et al., 2020; Levin et al., 2014; blue dice). According to the different timings on the proposed ancient seawater $\delta^{18}O$ initial values, (A) and (D) are modelled from 3.2 Ga to present day; (B), (C), (E), and (F) are modelled from 3.5 Ga to present day. Their corresponding crustal growth models (G-I) are tracked throughout the Earth's history.

It should be noted that the crustal evolution and thermal evolution of mantle are simulated throughout Earth history (Fig. 3A-C), whereas the evolution of seawater $\delta^{18}O$ and $\Delta'^{17}O$ is simulated from 3.24 Ga or 3.5 Ga to the present day (Fig. 3D and Fig. 4). There are two reasons behind this modeling scheme. First, as explained in the methods, f_{HT} and f_{LT} are constrained by the thermal evolution of the mantle and the surface mass balance of the carbon cycle. The thermal evolution of the mantle is well-constrained only from ~3.5 Ga to the present (Herzberg et al., 2010), whereas the early Earth condition is more uncertain. Second, the early carbon cycle is likely to have experienced considerable change during the Hadean to early Archean due to magma ocean solidification (e.g., Miyazaki and Korenaga, 2022); however, the details of this change remain ambiguous. Thus, we focus on the evolution of seawater $\delta^{18}O$ and $\Delta'^{17}O$ values from 3.5 Ga to the present when we have robust constraints, which is also the time span of the sedimentary $\delta^{18}O$ records to which we are comparing.

To understand how the crustal growth model is constrained after the aforementioned three stages, we compare the a posteriori distributions of model parameters with their a priori distributions (Fig. 5 and Figs. S2&S3). The distributions of crustal evolution parameters from stage 1 to 3 are shown in blue, gray, and red, respectively. The correlation coefficients between crustal growth parameters and all independent variables in thermal evolution and seawater $\delta^{18}O$ models are provided in Tables S6-S8. As described in section 2.3, we use six parameters to model continental evolution: the onset of crustal growth (t_s), the initial and present-day rates of crustal recycling (R_s and R_p), the decay constants of crustal recycling and growth rates (κ_r and κ_g), and the extent of crustal reworking (f_{rw}). The a priori ranges of these parameters are chosen following Rosas and Korenaga (2018), and the combinations of different parameter values allow us to model from convex to concave evolution patterns for crustal generation and recycling rates and to cover from late-stage to almost instantaneous crustal growth models.

As can be seen in Fig. 5, the first and second stages of Monte Carlo sampling do not provide tight bounds on crustal evolution, with most parameters exhibiting nearly uniform distributions (Fig. 5, A and D to F) and a slight preference to low recycling rate (Fig. 5, B and C). The a posteriori distributions after the first two stages cover the entire range of their a priori distributions (Table S5), which means all the proposed crustal growth models, ranging from early instant growth to late gradual growth, are tested during the seawater $\delta^{18}O$ model. The selection of early rapid continental growth is only due to the required driving forces of the rising seawater $\delta^{18}O$ during the Precambrian. As can be seen, the successful solutions from modeling seawater $\delta^{18}O$ values (third stage) strongly favor low present-day recycling rate R_p (Fig. 5B) and positive decay constants of crustal recycling κ_r (Fig. 5C), while slightly preferring high initial crustal recycling rate R_s (Fig. 5A). These results suggest favorable selection of crustal evolution with intense initial recycling followed by a rapid decrease. According to our formulation (equation (13)), the rate of crustal reworking is in sync with but lower than that of crustal recycling. Both recycling and reworking contribute to intense low-temperature crustal alteration in the early Earth (equation (6)), and consequently, a lower $\delta^{18}O$ value of seawater during the early Archean (Figs. 4 and S1). Net crustal growth is mainly controlled by κ_g, and ~94% of our successful solutions display κ_g larger than 3 Gyr^{-1}, indicating high crustal growth in the early Earth followed by a rapid decrease (Fig. 5D). Such a rapidly decreasing rate of crustal generation also facilitates the lowering of seawater $\delta^{18}O$ values during the early Archean (Fig. 4). The distributions of t_s and f_{rw} are rather uniform with some preference to later onset and higher reworking rate (Fig. 5, E and F). The significant contrasts between the a posteriori distributions from modeling seawater $\delta^{18}O$ values (third stage) and those from the previous stages suggest that the evolution of seawater $\delta^{18}O$ is sufficiently sensitive to different histories of continental formation, thereby providing a new constraint on crust-mantle differentiation.

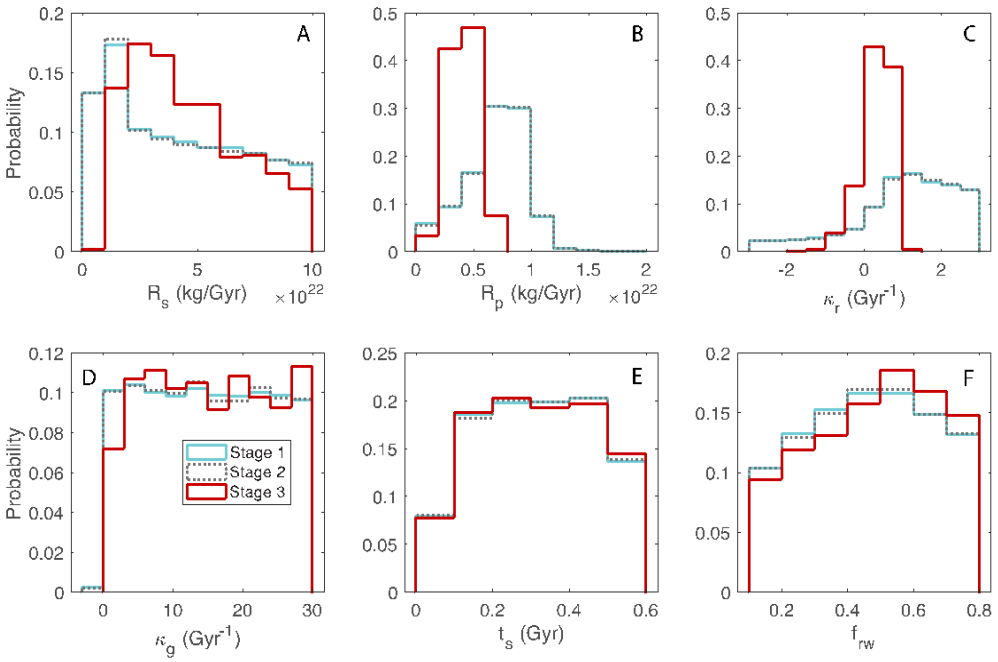

Fig. 5. The a posteriori distributions of crustal evolution parameters, based on ~$2x10^4$, ~$2.5x10^4$, and ~$3x10^3$ successful Monte Carlo solutions from stage 1 to 3 (for the initial conditions of seawater $\delta^{18}O$ is +3.3‰ at 3.24 Ga (Johnson and Wing, 2020)), respectively. Distributions from stage 1 to 3 are shown in green, blue, and red, respectively. (A) Initial recycling rate, (B) present-day recycling rate, (C) decay constant for crustal recycling, (D) decay constant for crustal generation, (E) onset time for crustal formation, and (F) reworking factor.

The model selected rates of crustal generation, recycling, and reworking and the evolution of plate velocity are shown in Fig. 6. It can be seen that the evolution of seawater $\delta^{18}O$ favors rapid continental growth with intense crustal recycling and reworking during the early Earth (Figs. 6A-C). The changing rates of crustal generation, recycling, and reworking display exponential decreases through time. According to our parameterization of the low-temperature alteration factor f_{LT} (equation (6)), such crustal formation history contributes to lowering f_{LT} since the Archean. Meanwhile, based on the thermal evolution of the mantle, the evolution of plate velocity exhibits an increase since the early Archean (Fig. 6D), which controls the rise of the high-temperature alteration factor f_{HT} (equation (3)). As explained in the Methods (Section 2), the exponent n in equation (3) determines the dependence of high-temperature alteration of oceanic crust on plate velocity, whose value can vary from 1 to 3. The successful Monte Carlo solutions suggest a strong preference to non-linear dependence, with ~ 70% results having a value of 3 (Fig. S4).

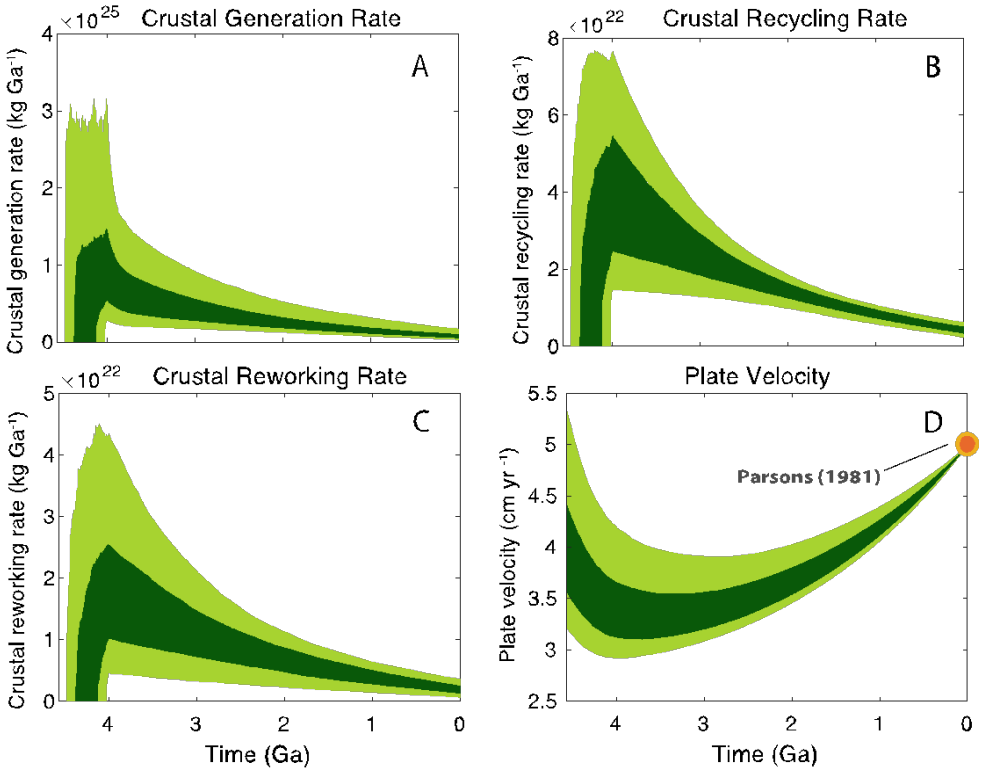

Fig. 6. Preferred crustal growth and thermal evolution based on ~3 x 10^3 successful Monte Carlo solutions. The middle 50% and 90% of successful solutions are shown in dark green and light green, respectively. The present-day plate velocity is from Parsons (1981). (A) Crustal generation rate (*Kmc*), (B) crustal recycling rate (*Krc*), (C) crustal reworking rate (*Krw*), and (D) plate velocity.

The evolving proportion of low- temperature (f_{LT}) and high-temperature (f_{HT}) crustal alterations are shown in Fig. 7, for the three scenarios with mid-Archean seawater $\delta^{18}O$ starting at +3.3‰, 0‰, and -13.3‰. The changing proportion of f_{LT} to f_{HT} determines the evolution of seawater $\delta^{18}O$ and $\Delta'^{17}O$ because the oxygen isotope composition of seawater is lowered by low-temperature alteration and increased by high-temperature alteration. The a posteriori distribution of isotope fractionation factors during Urey reaction (α_w), low-T alteration (α_{LT}), reverse weathering (α_{rev}), and high-T alteration (α_{HT}) are shown in Fig. S5. As can be seen from Fig. 7, the effect of f_{LT} displays a significant decrease through time, whereas f_{HT} shows a gentle but steady increase. As a result of these two competing processes, the effect of low-temperature alteration dominates the oxygen isotope exchange during the Archean for the first two scenarios (Figs. 7A-B), which causes the seawater $\delta^{18}O$ value to decrease to a possible minimum of -10‰ $\pm$ 2‰ (or ~-5‰, Fig. S1A-B) by the end of Archean (Figs. 4A-B). After that, however, a continued shift in the balance of high-temperature and low-temperature alteration causes a gradual increase of $\delta^{18}O$ throughout the

rest of Earth history. In similar fashion, their corresponding $\Delta'^{17}O$ values display an increase at the end of Archean and then a decrease through the Proterozoic (Figs. 4D-E and S1D-E), because low-temperature alteration increases $\Delta'^{17}O$ in seawater, whereas high-temperature alteration decreases it. For seawater $\delta^{18}O$ starting at -13.3‰, the shift of power between f_{LT} and f_{HT} is completed before 3.5 Ga, which results in high-temperature alteration always dominating and results in a steadily increasing seawater $\delta^{18}O$ value from 3.5Ga to modern (Figs. 4C and S1C). Consequently, the difference between f_{LT} and f_{HT} in Fig. 7C is smaller compared to Figs. 7A and B. With high-temperature alteration dominating most of the Earth history, the evolution of $\Delta'^{17}O$ values show a continuous decrease through time (Figs. 4F and 6F). The competing effect of f_{LT} and f_{HT} through time is also reflected in the evolution of $\lambda_{seawater}$, which displays an increasing trend through time as f_{HT} continuously increases (Fig. S6). These estimates of evolving f_{LT} and f_{HT} from the solid Earth evolution framework suggest that seawater $\delta^{18}O$ and $\Delta'^{17}O$ values may have changed considerably through time. Further, it is possible to reconstruct the proposed evolution of seawater $\delta^{18}O$ using a simple stochastic approach to explore the effect of a different range of options for solid Earth evolution.

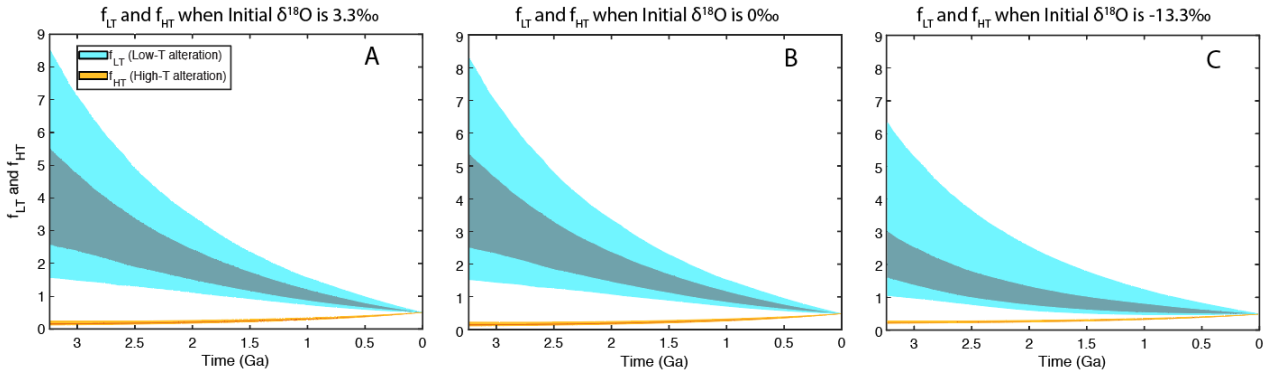

Fig. 7. Preferred evolution paths of high- and low-temperature alteration rates of oceanic crust (f_{HT} and f_{LT}) based on ~3 x 10^3 successful Monte Carlo solutions. (A) The f_{HT} and f_{LT} for the scenario of initial seawater is $\delta^{18}O$ is 3.3‰; (B) f_{HT} and f_{LT} when the initial seawater is $\delta^{18}O$ is 0‰; and (C) f_{HT} and f_{LT} when the initial seawater is $\delta^{18}O$ is -13.3‰. The parameters f_{HT} and f_{LT} are normalized by their respective present-day high- and low-temperature alteration rates. The middle 50% and 90% of successful solutions of f_{HT} are shown in dark orange and yellow, respectively, whereas those of successful solutions of f_{LT} are shown in dark blue and light blue, respectively.

4. Discussion

Consistent with previous models of seawater $\delta^{18}O$ evolution (e.g., Wallmann, 2001; Jaffrés et al., 2007; Johnson and Wing, 2020), our results show that the seawater oxygen isotope value can vary dramatically through time with solid Earth evolution. However, the magnitude of change is highly dependent on the ^{18}O mole fractionation of sedimentary rocks overtime, a value that is not well constrained through Earth history. Our approach delineates the trajectories of Earth system evolution that matches the $\delta^{18}O$ values recorded in sedimentary records, when assuming the sedimentary records are preserving precipitation conditions and have not undergone subsequent alteration (Zahkarov et al., 2021; Sengupta et al., 2020; Liljestrand et al., 2020; Galili et al., 2019; Bindeman et al., 2016; Prokoph et al., 2008; Levin et al., 2014; and references therein). Although the model results cannot clearly show whether the ocean $\delta^{18}O$ value was +3.3, 0, or -13‰ in the early Archean, all of our successful solutions are characterized by rapid early crustal growth with an exponential decrease in crustal generation, recycling, and reworking after the early Archean (Figs. 4 and 6). The preference for such rapid crustal formation is largely guided by the increase in seawater $\delta^{18}O$ during the Proterozoic. Since the $\Delta'^{17}O$ value is calculated based on the ratio of high- to low- temperature alteration flux, initial $\delta^{18}O$ and ϕ_{si} values do not impact the $\Delta'^{17}O$ seawater values from 2.5 Ga to modern. In all model outputs, the $\Delta'^{17}O$ value is about 0.015‰ $\pm$ 0.01‰ from 2.5 Ga and decreases to ~0‰ in the modern. This is considerably lower than previous model results of the $\Delta'^{17}O$ evolution of seawater (Sengupta et al, 2020; Liljestrand et al., 2020).

There has been a long-standing debate about the history of continental evolution (e.g., Armstrong, 1981; Campbell, 2003; Guo and Korenaga, 2018). Korenaga (2018) grouped various models of continental growth into three categories: crust-based, mantle-based, and others. Crust-based models are estimates on the present-day distribution of crustal formation age (e.g., Condie and Aster, 2010; Korenaga, 2018). They do not contain information of the crust that has been recycled into the mantle, thereby serving as the lower bound on net crustal growth. Mantle-based models utilize the complementary nature of the depleted mantle and the continental crust (e.g., Campbell, 2003; Rosas and Korenaga, 2018) and can constrain the net growth of continental crust. The third category (e.g., Pujol et al., 2013; Guo and Korenaga, 2020) uses less direct constraints than the mantle-based approach but still aims at constraining net continental growth. Our approach using the history of seawater $\delta^{18}O$ belongs to this third category. Assuming that the inferred history of seawater $\delta^{18}O$ are robust, the pattern of continental growth preferred by our modeling (Fig. 6)

552 is in good agreement with recent growth models based on Nd isotopes (Rosas and Korenaga, 2018)
553 and atmospheric argon (Guo and Korenaga, 2020), thereby reinforcing the notion of rapid crustal
554 growth during the Hadean and the early Archean.

555 A central feature of our model is the simultaneous application of multiple observational
556 constraints to ensure the internal consistency among crust-mantle differentiation, the thermal
557 evolution of the mantle, and the chemical evolution of the ocean . This treatment also allows us
558 to quantitatively investigate the changing proportion of low- to high-temperature alteration of
559 crustal materials through Earth history. As mentioned in the introduction, the products of low-
560 temperature alteration and silicate weathering are important sinks of heavy oxygen. In contrast,
561 high-temperature hydrothermal alteration does not intensively fractionate oxygen isotopes. The
562 relative proportion of these two competing processes controls the history of seawater $\delta^{18}O$ and
563 $\Delta'^{17}O$, which can be linked to mantle and crustal evolution.

564 Previous work on oxygen isotope values of seawater either focused on the evolution of
565 seawater $\delta^{18}O$ in the Phanerozoic (e.g., Wallmann, 2001) or modeled the evolution of f_{LT} to f_{HT} in
566 a simplified manner not directly grounded in geophysical modeling (e.g., Wallmann, 2001; Jaffrés
567 et al., 2007). For instance, it can be seen from Fig. 7 that, according to the thermal evolution of
568 mantle (e.g., Korenaga, 2018), the rate of high-temperature alteration does not exhibit an
569 exponential decrease through time as many papers assumed (e.g., Wallmann, 2001; Jaffrés et al.,
570 2007). By properly parameterizing f_{LT} and f_{HT}, our results suggest an alternative set of controls on
571 seawater oxygen isotopic composition — high-temperature alteration plays a leading role during
572 the Proterozoic due to the increasing plate velocity, whereas a possible domination of low-
573 temperature alteration before the end of Archean is caused by the significant amount of CO_2
574 released during crustal formation processes. The secular decrease of f_{LT} is mainly controlled by the
575 generation, recycling, and reworking rate of continental crust. These rates are checked against the
576 present-day distributions of continental crust formation (Korenaga, 2018) and surface age
577 distributions (Roberts and Spencer, 2015). On the other hand, the secular increase of f_{HT} is
578 informed by considering the sensitivity of mantle viscosity to both water and temperature. The
579 Earth's mantle was considerably hotter in the past compared to present, but a hotter mantle does
580 not necessarily result in more vigorous mantle convection (e.g., Korenaga, 2017). Considering also
581 the increasing water content in the mantle through Earth history (Korenaga et al., 2017), the
582 velocity of mantle convection should experience secular increase from ~3.5 Ga to present day,

583 which is further confirmed by empirical data of Herzberg et al. (2010). Our model provides a
584 comprehensive frame that provides another window into crust-mantle interactions, crustal growth,
585 and the chemical evolution of seawater.
586
587 **5. Conclusion**
588 We combined crustal evolution, thermal evolution, and oxygen isotope modeling and used a
589 stochastic approach to provide a new look at how seawater $\delta^{18}O$ and $\Delta'^{17}O$ values could change
590 through time. By doing this, we were able to delineate the possible path of Earth system evolution
591 that matches the $\delta^{18}O$ records in iron oxides, chert, shale, and carbonates (Zahkarov et al., 2021;
592 Sengupta et al., 2020; Liljestrand et al., 2020; Galili et al., 2019; Bindeman et al., 2016; Prokoph
593 et al., 2008; Levin et al., 2014; and references therein), although we were not able to explicitly
594 constrain the $\delta^{18}O$ value of early Archean seawater. Our results suggest that seawater $\delta^{18}O$ may
595 have increased from a possible minimum of ~-10‰ $\pm$ 2‰ (if ϕ_{si}= 2.017x10^{-3}) or ~-5‰ $\pm$ 2‰ (if
596 ϕ_{si}= 2.037x10^{-3}) at the end of Archean to the present-day value. The corresponding $\Delta'^{17}O$ may be
597 as high as ~0.015‰ $\pm$ 0.01‰ at the end of Archean and decreased with time. Using this approach,
598 we suggest that the considerable amount of CO_2 released during mantle magmatism and
599 continental recycling in the early Earth drives intense low-temperature alteration of oceanic crust
600 and silicate weathering, and as a result, lowers the seawater $\delta^{18}O$ and raises $\Delta'^{17}O$ values. After
601 the early Archean, the rates of crustal generation and recycling decrease, whereas plate velocity
602 continues to increase with time. As a result, the effect of high-temperature alteration starts to buffer
603 the low-temperature alteration flux, which raises seawater $\delta^{18}O$ and decreases $\Delta'^{17}O$ values. The
604 evolution of $\delta^{18}O$ values in seawater favors rapid continental growth in the early Earth, with the
605 crustal mass reaching its present-day level by the early Archean. The presence of a large amount
606 of continental crust in the early Earth has far-reaching implications for the onset of plate tectonics,
607 early surface environment, and the evolution of early life, thereby motivating further research to
608 test the proposed history of seawater $\delta^{18}O$.
609

Acknowledgements

This article was based on work supported by the National Science Foundation under grant EAR-1753916. N.J.P. recognizes support from NASA ICAR Alternative Earths Team. J.A.G.W recognizes support from NSF EAR-1952615.

Declaration of Competing Interest

The authors declare that they have no known competing financial interests or personal relationships that could have appeared to influence the work reported in this paper.

Author Contributions

M. G. performed the modeling and wrote the manuscript. J.A.G.W assisted with $\Delta'^{17}O$ modeling and commented on the manuscript. P. J. N. and J. K. designed the project, discussed the results, and commented on the manuscript.

Data statement

All data needed to evaluate the conclusions in the paper are present in the paper and/or the Supplementary Materials. The MATLAB scripts and data used in this study are provided at: https://github.com/MengGuo727/seawater-delta-18O.git.

628 **References**

629 Armstrong, R. L., Radiogenic isotopes: the case for crustal recycling on a near-steady-state no-
630 continent-growth Earth, *Phil. Tram. R. Soc. Lond. A*, **301**, 443-472 (1981). DOI:
631 https://doi.org/10.1098/rsta.1981.0122.

632 Bach, W., Humphris, S. E., Relationship between the Sr and O isotope compositions of
633 hydrothermal fluids and the spreading and magma-supply rates at oceanic spreading
634 centers. *Geology*, **27**, 1067-1070 (1999). DOI: https://doi.org/10.1130/0091-
635 7613(1999)027<1067:RBTSAO>2.3.CO;2.

636 Baker, E. T., German, C. R., On the global distribution of hydrothermal vent fields. Mid-Ocean
637 Ridges. In: German, C. R., Lin, J., Parson, L. M. (Eds.), *Hydrothermal Interactions*
638 *Between the Lithosphere and Oceans*, *Geophys. Monogr. Ser*, **148**, 245-266 (2004). DOI:
639 https://doi.org/10.1029/148GM10.

640 Baker, E. T., Relationships between hydrothermal activity and axial magma chamber distribution,
641 depth, and melt content. *Geochem., Geophys., Geosyst.,* **10** (2009). DOI:
642 https://doi.org/10.1029/2009GC002424.

643 Bindeman, I. N., Bekker, A., Zakharov, D. O., Oxygen isotope perspective on crustal evolution on
644 early Earth: A record of Precambrian shales with emphasis on Paleoproterozoic glaciations
645 and Great Oxygenation Event. *Earth Planet. Sci. Lett.*, **437**, 101-113 (2016). DOI:
646 https://doi.org/10.1016/j.epsl.2015.12.029.

647 Campbell, I. H., Constraints on continental growth models from Nb/U ratios in the 3.5 Ga
648 Barberton and other Archaean basalt-komatiite suites. *Am. J. Sci.* **303**, 319-351 (2003).
649 DOI: https://doi.org/10.2475/ajs.303.4.319.

650 Cao, X., Liu, Y., Equilibrium mass-dependent fractionation relationships for triple oxygen
651 isotopes. *Geochim. Cosmochim. Acta*, **75**, 7435-7445 (2011). DOI:
652 https://doi.org/10.1016/j.gca.2011.09.048.

653 Chen, Y. J., Modeling the thermal state of the oceanic crust. In: German, C. R., Lin, J., Parson, L.
654 M. (Eds.), *Hydrothermal Interactions Between the Lithosphere and Oceans, Geophys.*
655 *Monogr. Ser.*, **148**, 95-110 (2004). DOI: 10.1029/148GM04.

656 Condie, K. C., Aster, R. C., Episodic zircon age spectra of orogenic granitoids: the supercontinent
657 connection and continental growth. *Precambrian Res.,* **180**, 227-236 (2010). DOI:
658 https://doi.org/10.1016/j.precamres.2010.03.008.

659 Coogan, L. A., Gillis, K. M., The average Phanerozoic CO_2 degassing flux estimated from the O-
660 isotopic composition of seawater. *Earth Planet. Sci. Lett.*, ***536***, 116151 (2020). DOI:
661 https://doi.org/10.1016/j.epsl.2020.116151.
662 Galili, N., Shemesh, A., Yam, R., Brailovsky, I., Sela-Adler, M., Schuster, E. M., Collom, C.,
663 Bekker, A., Planavsky, N., Macdonald, F. A., Préat, A., Rudmin, M., Trela, W., Sturesson,
664 U., Heikoop, J. M., Aurell, M., Ramajo, J., Halevy, I., The geologic history of seawater
665 oxygen isotopes from marine iron oxides. *Science*, **365**, 469-473 (2019). DOI:
666 10.1126/science.aaw9247.
667 German, C. R., Parson, L. M., Distributions of hydrothermal activity along the Mid-Atlantic Ridge:
668 interplay of magmatic and tectonic controls. *Earth Planet. Sci. Lett.*, **160**, 327-341 (1998).
669 DOI: https://doi.org/10.1016/S0012-821X(98)00093-4.
670 Guo, M., Korenaga, J., Argon constraints on the early growth of felsic continental crust. *Sci.*
671 *Adv.*, ***6***, eaaz6234 (2020). DOI: 10.1126/sciadv.aaz6234.
672 Herwartz, D., Pack, A., Nagel, T. J., A CO2 greenhouse efficiently warmed the early Earth and
673 decreased seawater 18O/16O before the onset of plate tectonics. *Proc. Natl. Acad. Sci.*
674 *U.S.A*, **118** (2021). DOI: https://doi.org/10.1073/pnas.2023617118.
675 Herzberg, C., Condie, K., Korenaga, J., Thermal history of the Earth and its petrological
676 expression. *Earth Planet. Sci. Lett.,* **292**, 79-88 (2010). DOI:
677 https://doi.org/10.1016/j.epsl.2010.01.022.
678 Holland, G., Ballentine, C. J., Seawater subduction controls the heavy noble gas composition of
679 the mantle. *Nature*, **441**, 186-191 (2006). DOI:10.1038/nature04761.
680 Isson, T. T., Planavsky, N. J., Reverse weathering as a long-term stabilizer of marine pH and
681 planetary climate. *Nature*, **560**, 471-475 (2018). DOI: https://doi.org/10.1038/s41586-018-
682 0408-4.
683 Jaffrés, J. B., Shields, G. A., Wallmann, K., The oxygen isotope evolution of seawater: A critical
684 review of a long-standing controversy and an improved geological water cycle model for
685 the past 3.4 billion years. *Earth Sci. Rev.,* **83**, 83–122 (2007). DOI:
686 https://doi.org/10.1016/j.earscirev.2007.04.002.
687 Jaupart, C., Labrosse, S., Mareschal, J. C., "Temperatures, heat and energy in the mantle of the
688 Earth" in *Treatise on Geophysics Vol. 7,* Eds. Schubert, G. (Elsevier, 2007), pp. 253-303.
689 DOI:10.1016/B978-0-444-53802-4.00126-3.

690 Johnson, B. W., Wing, B. A., Limited Archaean continental emergence reflected in an early
691 Archaean ^{18}O-enriched ocean. *Nature Geosci.*, **13**, 243-248 (2020). DOI:
692 https://doi.org/10.1038/s41561-020-0538-9.
693 Knauth, L. P., Epstein, S., Hydrogen and oxygen isotope ratios in nodular and bedded cherts.
694 *Geochim. Cosmochim. Acta*, **40**, 1095-1108 (1976). DOI: https://doi.org/10.1016/0016-
695 7037(76)90051-X.
696 Korenaga, J., Archean geodynamics and the thermal evolution of Earth. In *Archean Geodynamics*
697 *and Environments*, *AGU Geophys. Monogr. Ser.*, **164**, 7 (2006). DOI:
698 https://doi.org/10.1029/164GM03.
699 Korenaga, J., Thermal evolution with a hydrating mantle and the initiation of plate tectonics in the
700 early Earth. *J. Geophys. Res. Solid Earth*, **116** (2011). DOI:
701 https://doi.org/10.1029/2011JB008410.
702 Korenaga, J., Pitfalls in modeling mantle convection with internal heat production, *J. Geophys.*
703 *Res. Solid Earth*, **122**, 4064-4085 (2017). DOI: 10.1002/2016JB013850.
704 Korenaga, J., Planavsky, N. J., Evans, D. A. D., Global water cycle and the coevolution of Earth's
705 interior and surface environment, *Phil. Trans. R. Soc. A*, **375**, 20150393 (2017).
706 DOI:10.1098/rsta.2015.0393.
707 Korenaga, J., Estimating the formation age distribution of continental crust by unmixing zircon
708 ages. *Earth Planet. Sci. Lett.,* **482**, 388-395 (2018). DOI:
709 https://doi.org/10.1016/j.epsl.2017.11.039.
710 Korenaga, J., Crustal evolution and mantle dynamics through Earth history, *Phil. Trans. R. Soc.*
711 *A,* **376**, 20170408 (2018). DOI: http://dx.doi.org/10.1098/rsta.2017.0408.
712 Levin, N. E., Raub, T. D., Dauphas, N., Eiler, J. M., Triple oxygen isotope variations in
713 sedimentary rocks. *Geochim. Cosmochim. Acta*, **139**, 173-189 (2014). DOI:
714 https://doi.org/10.1016/j.gca.2014.04.034.
715 Liljestrand, F. L., Knoll, A. H., Tosca, N. J., Cohen, P. A., Macdonald, F. A., Peng, Y., Johnston,
716 D. T., The triple oxygen isotope composition of Precambrian chert. *Earth Planet. Sci. Lett.,*
717 **537**, 116167 (2020). DOI: https://doi.org/10.1016/j.epsl.2020.116167.
718 Lowe, D. R., Ibarra, D. E., Drabon, N., Chamberlain, C. P., Constraints on surface temperature 3.4
719 billion years ago based on triple oxygen isotopes of cherts from the Barberton Greenstone

720 Belt, South Africa, and the problem of sample selection. *Am. J. Sci.*, **320**, 790-814 (2020).
721 DOI: https://doi.org/10.2475/11.2020.02.
722 Mei, S., Kohlstedt, D. L., Influence of water on plastic deformation of olivine aggregates: 1.
723 Diffusion creep regime. *J. Geophys. Res. Solid Earth*, **105**, 21457-21469 (2000). DOI:
724 https://doi.org/10.1029/2000JB900179.
725 Miyazaki, Y., Korenaga, J., A wet heterogeneous mantle creates a habitable world in the Hadean.
726 *Nature*, **603,** 86-90 (2022). DOI: https://doi.org/10.1038/s41586-021-04371-9.
727 Muehlenbachs, K., The oxygen isotopic composition of the oceans, sediments and the
728 seafloor. *Chem. Geol.*, 145(3-4), 263-273 (1998). DOI: https://doi.org/10.1016/S0009-
729 2541(97)00147-2.
730 Muehlenbachs, K., Furnes, H., Fonneland, H. C., Hellevang, B., Ophiolites as faithful records of
731 the oxygen isotope ratio of ancient seawater: the Solund-Stavfjord Ophiolite Complex as a
732 Late Ordovician example. In *Ophiolites in Earth History, Geol. Soc. London Spec. Pub*.
733 **218**, 401–414 (2003). DOI: https://doi.org/10.1144/GSL.SP.2003.218.01.20.
734 O'Rourke, J. G., Korenaga, J., Stevenson, D. J., Thermal evolution of Earth with magnesium
735 precipitation in the core. *Earth Planet. Sci. Lett.,* **458**, 263-272 (2017). DOI:
736 https://doi.org/10.1016/j.epsl.2016.10.057.
737 Parsons, B., The rates of plate creation and consumption. *Geophys. J. Int.* **67**, 437-448 (1981).
738 DOI: https://doi.org/10.1111/j.1365-246X.1981.tb02759.x.
739 Phipps Morgan, J., Chen, Y. J., The genesis of oceanic crust: Magma injection, hydrothermal
740 circulation, and crustal flow. *J. Geophys. Res. Solid Earth*, **98**, 6283-6297 (1993). DOI:
741 https://doi.org/10.1029/92JB02650.
742 Plank, T., Manning, C. E., Subducting carbon. *Nature,* **574**, 343-352 (2019). DOI:
743 https://doi.org/10.1038/s41586-019-1643-z.
744 Pope, E. C., Bird, D. K., Rosing, M. T., Isotope composition and volume of Earth's early
745 oceans. *PNAS*, **109,** 4371-4376 (2012). DOI: https://doi.org/10.1073/pnas.1115705109.
746 Prokoph, A., Shields, G. A., Veizer, J., Compilation and time-series analysis of a marine carbonate
747 $\delta^{18}O$, $\delta^{13}C$, $^{87}Sr/^{86}Sr$ and $\delta^{34}S$ database through Earth history. *Earth Sci. Rev.*, **87**, 113-133.
748 DOI: https://doi.org/10.1016/j.earscirev.2007.12.003 (2008).

749 Pujol, M., Marty, B., Burgess, R., Turner, G., Philippot, P., Argon isotopic composition of
750 Archaean atmosphere probes early Earth geodynamics. *Nature,* **498**, 87 (2013). DOI:
751 10.1038/nature12152.
752 Robert, F., Chaussidon, M., A palaeotemperature curve for the Precambrian oceans based on
753 silicon isotopes in cherts. *Nature*, **443**, 969–972 (2006). DOI: 10.1038/nature05239.
754 Roberts, N. M. W., Spencer, C. J., The zircon archive of continent formation through time. In:
755 Roberts, N. M. W., Van Kranendonk, M., Parman, S., Shirey, S., Clift, P. D. (Eds.),
756 *Continent Formation Through Time, Geol. Soc. London Spec. Pub.,* **389**, 197-225 (2015).
757 DOI: https://doi.org/10.1144/SP389.14.
758 Rosas, J. C., Korenaga, J., Rapid crustal growth and efficient crustal recycling in the early Earth:
759 Implications for Hadean and Archean geodynamics. *Earth Planet. Sci. Lett.,* **494,** 42-49
760 (2018). DOI: https://doi.org/10.1016/j.epsl.2018.04.051.
761 Rudnick, R. L., Gao, S., "Composition of the Continental Crust" in *Treatise on Geochemistry,* **Vol.**
762 **4**, Eds. Holland, H. D., Turekian, K. K. (Pergamon, 2014), pp. 1–51. DOI:
763 https://doi.org/10.1016/B978-0-08-095975-7.00301-6.
764 Stern, R. J., Scholl, D. W., Yin and yang of continental crust creation and destruction by plate
765 tectonic processes. *Int. Geol. Rev.,* **52**, 1-31 (2010). DOI:
766 https://doi.org/10.1080/00206810903332322.
767 Sengupta, S., Peters, S. T., Reitner, J., Duda, J. P., Pack, A. Triple oxygen isotopes of cherts
768 through time. *Chem. Geol.*, **554**, 119789 (2020). DOI:
769 https://doi.org/10.1016/j.chemgeo.2020.119789.
770 Walker, J. C. G., Lohmann, K. C., Why the oxygen isotopic composition of sea water changes
771 with time. *Geophys. Res. Lett.*, **16**, 323–326 (1989). DOI:
772 https://doi.org/10.1029/GL016i004p00323.
773 Wallmann, K., The geological water cycle and the evolution of marine $\delta^{18}O$ values. *Geochim.*
774 *Cosmochim. Acta*, **65**, 2469-2485 (2001). DOI: https://doi.org/10.1016/S0016-
775 7037(01)00603-2.
776 Wostbrock, J. A., Sharp, Z. D., Triple oxygen isotopes in silica–water and carbonate–water
777 systems. *Rev. Mineral. Geochem*., **86**, 367-400 (2021). DOI:
778 https://doi.org/10.2138/rmg.2021.86.11.

779 Zakharov, D. O., Marin-Carbonne, J., Alleon, J., Bindeman, I. N. Triple oxygen isotope trend
780 recorded by Precambrian cherts: A perspective from combined bulk and in situ secondary
781 ion probe measurements. *Rev. Mineral. Geochem.*, **86**, 323-365 (2021). DOI:
782 https://doi.org/10.2138/rmg.2021.86.10.

Supplementary material

Table. S1. The mass balances relationships considered in seawater $\delta^{18}O$ model (following Wallmann (2001)).

Reservoirs	Differential Equations
Changing O mass in free water	$\frac{dM_{fw}}{dt} = [F_{reHT}(t) + F_{reLT}(t) + F_{rew}(t) + F_m(t)] - [F_{HT}(t) + F_{LT}(t) + F_w(t) + F_{rev}(t)]$
Changing ^{18}O mass in free water	$\frac{dM^{18}_{fw}}{dt} = [F^{18}_{reHT}(t) + F^{ex}_{HT}(t) + F^{18}_{reLT}(t) + F^{ex}_{LT}(t) + F^{ex}_{w}(t) + F^{ex}_{rev}(t) + F^{18}_{rew}(t) + F^{18}_{m}(t)] - [F^{18}_{HT}(t) + F^{18}_{LT}(t) + F^{18}_{w}(t) + F^{18}_{rev}(t)]$
Changing mass of ^{18}O bonded in high-T altered OC	$\frac{dM^{18}_{HT}}{dt} = [F^{18}_{HT}(t) + F^{18}_{mHT}(t)] - [F^{18}_{reHT}(t) + F^{ex}_{HT}(t) + F^{18}_{sHT}(t)]$
Changing mass of ^{18}O bonded in low-T altered OC	$\frac{dM^{18}_{up}}{dt} = [F^{18}_{LT}(t) + F^{18}_{mLT}(t)] - [F^{18}_{reLT}(t) + F^{ex}_{LT}(t) + F^{18}_{sLT}(t)]$
Changing mass of ^{18}O bonded in sediments	$\frac{dM^{18}_{w}}{dt} = [F^{18}_{w}(t) + F^{18}_{rev}(t) + F^{18}_{mw}(t)] - [F^{ex}_{w}(t) + F^{ex}_{rev}(t) + F^{18}_{rew}(t) + F^{18}_{sw}(t)]$

Table. S2. Parameterization of the mass transfer rates considered in seawater $\delta^{18}O$ model (following Wallmann (2001)).

Mass transfer rates	Parameterizations
O fixation in high-T altered OC	$F_{HT}(t) = f_{HT}(t)\, F_{HT}(t_0)$
O fixation in low-T altered OC	$F_{LT}(t) = f_{LT}(t)\, \frac{V(t)}{V(t_p)} F_{LT}(t_0)$
O fixation in sediments during Urey reaction	$F_w(t) = f_{LT}(t)\, \frac{K_{rc}(t)}{K_{rc}(t_p)} F_w(t_0)$
O fixation in sediments during reverse weathering	$F_{rev}(t) = f_{rev}(t)\, (F_{LT}(t) + F_w(t))$
O released from mantle at spreading center	$F_m(t) = \frac{K_{mo}(t) + K_{mp}(t)}{K_{mo}(t_p) + K_{mp}(t_p)} F_m(t_0)$
O released from high-T altered OC during subduction	$F_{reHT}(t) = r(t)\, F_{HT}(t)$
O released from low-T altered OC during subduction	$F_{reLT}(t) = r(t)\, F_{LT}(t)$
O released from sediments during subduction	$F_{rew}(t) = r(t)\, (F_w(t) + F_{rev}(t))$
^{18}O fixation in high-T altered OC	$F^{18}_{HT}(t) = \frac{\alpha_{HT} R_f(t)}{1 + \alpha_{HT} R_f(t)} F_{HT}(t)$
^{18}O fixation in low-T altered OC	$F^{18}_{LT}(t) = \frac{\alpha_{LT} R_f(t)}{1 + \alpha_{LT} R_f(t)} F_{LT}(t)$
^{18}O fixation in sediments during Urey reaction	$F^{18}_{w}(t) = \frac{\alpha_{w} R_f(t)}{1 + \alpha_{w} R_f(t)} F_{w}(t)$
^{18}O fixation in sediments during reverse weathering	$F^{18}_{rev}(t) = \frac{\alpha_{rev} R_f(t)}{1 + \alpha_{rev} R_f(t)} F_{rev}(t)$
^{18}O released from mantle at spreading center	$F^{18}_{m}(t) = \phi_m\, F_m(t)$
^{18}O released from high-T altered OC during subduction	$F^{18}_{reHT}(t) = \phi_{HT}(t)\, F_{reHT}(t)$
^{18}O released from low-T altered OC during subduction	$F^{18}_{reLT}(t) = \phi_{LT}(t)\, F_{reLT}(t)$
^{18}O released from sediments during subduction	$F^{18}_{rew}(t) = \phi_{w}(t)\, F_{rew}(t)$
^{18}O exchanged between high-T altered OC and seawater	$F^{ex}_{HT}(t) = f_{HT}(t)\, k_{HT}\, (\Omega_{HT}(t) - 1)$
^{18}O exchanged between low-T altered OC and seawater	$F^{ex}_{LT}(t) = f_{LT}(t)\, k_{LT}\, (\Omega_{LT}(t) - 1)$
^{18}O exchanged during Urey reaction	$F^{ex}_{w}(t) = f_{LT}(t)\, k_{w}\, (\Omega_{w}(t) - 1)$
^{18}O exchanged during reverse weathering	$F^{ex}_{rev}(t) = f_{rev}(t) f_{LT}(t)\, k_{w}\, (\Omega_{rev}(t) - 1)$
Formation of ^{18}O in high-T altered OC at spreading center	$F^{18}_{mHT}(t) = \phi_{oc}\, f_{HT}(t)\, F_{mHT}(t_0)$
Formation of ^{18}O in low-T altered OC at spreading center	$F^{18}_{mLT}(t) = \phi_{oc}\, f_{LT}(t)\, F_{mLT}(t_0)$

Formation of ^{18}O in sediments at subduction zone	
Subduction of ^{18}O in high-T altered OC at spreading center	$F_{sHT}^{18}(t) = \phi_{HT}(t)\, f_{HT}(t)\, F_{mHT}(t_0) + \phi_{HT}(t)\,(1 - r_{HT}(t))\, F_{HT}(t)$
Subduction of ^{18}O in low-T altered OC at spreading center	$F_{sLT}^{18}(t) = \phi_{LT}(t)\, f_{LT}(t)\, F_{mLT}(t_0) + \phi_{LT}(t)(1 - r_{LT}(t))\, F_{LT}(t)$
Subduction of ^{18}O in sediments	$F_{sw}^{18}(t) = \phi_{w}(t)\, f_{LT}(t)\, F_{pw}(t_0) + \phi_{w}(t)\,(1 - r_{w}(t))\, F_{w}(t)$

Table. S3. The dependent parameters in seawater $\delta^{18}O$ model (following Wallmann (2001)).

Dependent parameters	Parameterizations
^{18}O mole fraction in high-T altered OC	$\phi_{HT}(t) = \frac{M_{HT}^{18}(t)}{M_{HT}(t)}$
^{18}O mole fraction in low-T altered OC	$\phi_{LT}(t) = \frac{M_{LT}^{18}(t)}{M_{LT}(t)}$
^{18}O mole fraction in sediments	$\phi_{w}(t) = \frac{M_{w}^{18}(t)}{M_{w}(t)}$
^{18}O mole fraction in free water	$\phi_{f}(t) = \frac{M_{fw}^{18}(t)}{M_{fw}(t)}$
$\frac{18O}{16O}$ ratios in each reservoir	$R(t) = \frac{\phi(t)}{1 - \phi(t)}$
Isotopic saturation index of ^{18}O exchange in high-T altered OC	$\Omega_{HT}(t) = \frac{R_{oc}}{\alpha_{HT} R_f(t)}$
Isotopic saturation index of ^{18}O exchange in low-T altered OC	$\Omega_{LT}(t) = \frac{R_{oc}}{\alpha_{LT} R_f(t)}$
Isotopic saturation index of ^{18}O exchange during Urey reaction	$\Omega_{w}(t) = \frac{R_{si}}{\alpha_{w} R_f(t)}$
Isotopic saturation index of 18O exchange during reverse weathering	$\Omega_{rev}(t) = \frac{R_{si}}{\alpha_{rev} R_f(t)}$

795 Table. S4. The constants and values used in seawater $\delta^{18}O$ model (following Wallmann (2001)).

Parameters	Values used in the Model
Present-day O fixation in high-T altered OC	$F_{HT}(t_0) = 20$ -70 x 10^{18} mol/Myr
Present-day O fixation in low-T altered OC	$F_{LT}(t_0) = 6$ x 10^{18} mol/Myr
Present-day O fixation in sediments during Urey reaction	$F_w(t_0) = 7$ x 10^{18} mol/Myr
Present-day O released from mantle at spreading center	$F_m(t_0) = 3$ x 10^{18} mol/Myr
Present-day formation rate of ^{18}O in high-T altered OC at spreading center	$F_{mHT}(t_0) = 1.6$ x 10^{21} mol/Myr
Present-day formation rate of ^{18}O in low-T altered OC at spreading center	$F_{mLT}(t_0) = 1.2$ x 10^{20} mol/Myr
Present-day formation rate of ^{18}O in sediments at spreading center	$F_{mw}(t_0) = 7.8$ x 10^{19} mol/Myr
The proportion of reverse weathering to low-temperature alteration and weathering processes (nondimensional)	$f_{rev}(t) = 20 \pm 5\%$
Recycle factor of oxygen at subduction zones	$r = 0\ to\ 1$
Isotopic fractionation for O fixation in high-T altered OC	$\alpha_{HT} = 1$ to 1.01
Isotopic fractionation for O fixation in low-T altered OC	$\alpha_{LT} = 1.015 \pm 0.003$
Isotopic fractionation for O fixation in sediments during Urey reaction	$\alpha_w = 1.020 \pm 0.003$
Isotopic fractionation for O fixation in mantle	$\alpha_m = 1$ to 1.01
Isotopic fractionation for O fixation during reverse weathering	$\alpha_{rev} = 1.025 \pm 0.003$
θ value for low-T alteration	$\theta_{LT} = 0.524$ to 0.525
θ value for mid-T alteration	$\theta_{MT} = 0.525$ to 0.526
θ value for high-T alteration	$\theta_{HT} = 0.527$ to 0.528
θ value for mantle condition	$\theta_m = 0.528$ to 0.529
Kinetic constant for isotopic exchange in high-T altered OC	$k_{HT} = 4.8$ x 10^{17} mol ^{18}O /Myr
Kinetic constant for isotopic exchange in low-T altered OC	$k_{LT} = 1.0$x 10^{17} mol ^{18}O /Myr
Kinetic constant for isotopic exchange in sediments weathering	$k_w = 1.2$ x 10^{17} mol ^{18}O /Myr
^{18}O mole fraction in fresh oceanic crust	$\phi_{oc} = 2.0126$ x 10^{-3}
^{18}O mole fraction in weathered silicate rocks	$\phi_{si} = 2.017$ and 2.032 x 10^{-3}
^{18}O mole fraction in mantle	$\phi_m = 2.015$ x 10^{-3}
Mass of oxygen in high-T altered OC	$M_{HT} = 1.68$ x 10^{23} mole
Mass of oxygen in low-T altered OC	$M_{LT} = 1.0$x 10^{22} mole
Mass of oxygen in sediments	$M_w = 7.0$ x 10^{22} mole

796
797

Table S5. The independent parameters in crustal evolution (following Guo and Korenaga (2020)), thermal evolution (following Guo and Korenaga (2020)), and seawater $\delta^{18}O$ model.

Parameter	Definition	Value	Unit
κ_r	Decay constant of crustal recycling rate	-3 to 3	Gyr $^{-1}$
κ_g	Decay constant of crustal generation rate	-1 to 30	Gyr $^{-1}$
R_s	Initial crustal recycling rate	0 to 10 x 10^{22}	kg Gyr $^{-1}$
R_p	Present-day crustal recycling rate	0 to 2 x 10^{22}	kg Gyr $^{-1}$
t_s	Crustal growth starting point	0.057 to 0.567	Gyr
f_{rw}	Crustal reworking rate factor	0.1 to 0.8	-
$H_{BSE}(t_p)$	Present-day BSE heat production	13 to 19	TW
$H_{CC}(t_p)$	Present-day continental crust heat production	5 to 10	TW
$Q_{total}(t_p)$	Present-day total terrestrial heat flux	43 to 49	TW
$Q_c(t_p)$	Present-day core heat flux	5 to 15	TW
ΔQ_c	Difference between initial and present-day Q_c	2 to 5	TW
n	Exponent in equation (3), which describes the dependence of high-temperature alteration of oceanic crust on plate velocity	1 to 3	-

Table S6. The correlation matrix of independent variables in crustal growth, thermal evolution, and seawater $\delta^{18}O$ models, for the initial condition of seawater $\delta^{18}O$ is +3.3‰ at 3.24 Ga (Johnson and Wing, 2020).

	f_{rw}	κ_r	κ_g	R_s	R_p	t_s	$H_{BSE}(t_p)$	$H_{CC}(t_p)$	$Q_{total}(t_p)$	$Q_c(t_p)$	ΔQ_c	f_{rev}	r	α_w	α_{LT}	α_{rev}	α_{HT}	$\phi_w(t_0)$	$\phi_{LT}(t_0)$	$\phi_{HT}(t_0)$	$\phi_f(t_0)$	n	$F_{HT}(t_0)$	θ_{LT}	θ_{MT}	θ_{HT}
f_{rw}	1.00	0.14	-0.01	0.05	-0.25	0.03	0.08	-0.02	0.02	-0.04	0.03	0.05	0.01	0.01	0.02	-0.01	0.01	0.10	-0.02	0.04	-0.05	0.10	-0.02	0.02	0.03	-0.09
κ_r	0.14	1.00	0.06	0.78	0.26	0.01	0.01	0.07	0.01	-0.06	-0.05	0.20	-0.05	0.12	0.02	-0.05	-0.06	0.03	0.01	0.00	-0.10	0.23	0.05	-0.01	0.07	-0.02
κ_g	-0.01	0.06	1.00	0.01	0.09	-0.06	0.07	0.09	0.04	-0.02	-0.08	0.08	-0.10	0.04	-0.08	0.04	-0.11	0.05	-0.05	0.07	-0.04	-0.03	-0.03	-0.05	0.03	0.00
R_s	0.05	0.78	0.01	1.00	0.29	-0.12	-0.07	0.08	-0.04	-0.06	-0.07	0.09	0.14	0.04	0.09	-0.04	-0.09	-0.01	0.00	-0.01	-0.09	0.15	0.07	0.01	0.13	-0.04
R_p	-0.25	0.26	0.09	0.29	1.00	0.01	-0.06	0.12	0.09	-0.10	-0.04	0.04	-0.43	0.12	0.03	-0.06	0.16	0.02	0.06	-0.02	-0.07	0.07	-0.03	0.00	0.08	0.08
t_s	0.03	0.01	-0.06	-0.12	0.01	1.00	0.00	0.00	0.07	0.09	-0.01	-0.09	0.00	0.10	-0.07	-0.04	0.04	-0.07	-0.02	0.08	-0.07	0.08	0.05	0.04	-0.07	0.01
$H_{BSE}(t_p)$	0.08	0.01	0.07	-0.07	-0.06	0.00	1.00	0.12	0.18	-0.44	0.01	0.06	-0.07	0.00	0.04	-0.05	-0.12	0.01	0.09	0.01	-0.04	0.08	-0.03	0.10	-0.10	-0.09
$H_{CC}(t_p)$	-0.02	0.07	0.09	0.08	0.12	0.00	0.12	1.00	-0.12	0.05	0.09	0.04	0.01	0.09	0.07	-0.11	-0.02	0.03	-0.01	-0.06	-0.06	-0.05	-0.10	0.09	0.03	-0.05
$Q_{total}(t_p)$	0.02	0.01	0.04	-0.04	0.09	0.07	0.18	-0.12	1.00	0.26	-0.04	-0.05	-0.22	0.00	0.03	0.00	0.14	0.04	0.04	0.05	0.07	-0.03	-0.01	-0.15	-0.07	0.04
$Q_c(t_p)$	-0.04	-0.06	-0.02	-0.06	-0.10	0.09	-0.44	0.05	0.26	1.00	0.00	-0.02	0.08	0.15	0.02	0.04	-0.12	-0.01	-0.10	0.05	0.04	0.03	-0.01	-0.06	0.03	-0.04
ΔQ_c	0.03	-0.05	-0.08	-0.07	-0.04	-0.01	0.01	0.09	-0.04	0.00	1.00	-0.09	0.00	0.01	0.06	0.00	0.06	0.16	-0.04	0.06	-0.03	0.04	0.01	-0.04	-0.02	-0.12
f_{rev}	0.05	0.20	0.08	0.09	0.04	-0.09	0.06	0.04	-0.05	-0.02	-0.09	1.00	0.06	-0.28	-0.16	-0.12	-0.26	0.06	-0.04	0.07	-0.03	-0.10	-0.29	-0.10	-0.03	0.09
r	0.01	-0.05	-0.10	0.14	-0.43	0.00	-0.07	0.01	-0.22	0.08	0.00	0.06	1.00	-0.13	-0.01	-0.03	-0.03	-0.06	-0.05	0.00	-0.04	-0.03	0.01	0.10	0.04	0.04
α_w	0.01	0.12	0.04	0.04	0.12	0.10	0.00	0.09	0.00	0.15	0.01	-0.28	-0.13	1.00	-0.25	0.01	0.11	-0.03	0.11	0.10	0.03	-0.17	-0.27	0.04	-0.02	-0.03
α_{LT}	0.02	0.02	-0.08	0.09	0.03	-0.07	0.04	0.07	0.03	0.02	0.06	-0.16	-0.01	-0.25	1.00	-0.06	0.00	0.03	-0.01	-0.03	-0.04	-0.12	-0.12	-0.01	0.07	0.01
α_{rev}	-0.01	-0.05	0.04	-0.04	-0.06	-0.04	-0.05	-0.11	0.00	0.04	0.00	-0.12	-0.03	0.01	-0.06	1.00	-0.06	0.01	-0.10	0.04	0.08	-0.07	-0.06	-0.05	0.05	-0.04
α_{HT}	0.01	-0.06	-0.11	-0.09	0.16	0.04	-0.12	-0.02	0.14	-0.12	0.06	-0.26	-0.03	0.11	0.00	-0.06	1.00	-0.03	0.13	0.02	0.01	0.17	-0.16	-0.11	-0.05	0.04
$\phi_w(t_0)$	0.10	0.03	0.05	-0.01	0.02	-0.07	0.01	0.03	0.04	-0.01	0.16	0.06	-0.06	-0.03	0.03	0.01	-0.03	1.00	0.01	0.04	0.08	0.09	0.00	0.03	0.05	-0.02
$\phi_{LT}(t_0)$	-0.02	0.01	-0.05	0.00	0.06	-0.02	0.09	-0.01	0.04	-0.10	-0.04	-0.04	-0.05	0.11	-0.01	-0.10	0.13	0.01	1.00	0.01	0.11	0.04	-0.11	-0.01	0.00	-0.13
$\phi_{HT}(t_0)$	0.04	0.00	0.07	-0.01	-0.02	0.08	0.01	-0.06	0.05	0.05	0.06	0.07	0.00	0.10	-0.03	0.04	0.02	0.04	0.01	1.00	-0.05	-0.04	-0.02	0.01	-0.06	0.02
$\phi_f(t_0)$	-0.05	-0.10	-0.04	-0.09	-0.07	-0.07	-0.04	-0.06	0.07	0.04	-0.03	-0.03	-0.04	0.03	-0.04	0.08	0.01	0.08	0.11	-0.05	1.00	0.01	0.01	0.05	0.05	0.03
n	0.10	0.23	-0.03	0.15	0.07	0.08	0.08	-0.05	-0.03	0.03	0.04	-0.10	-0.03	-0.17	-0.12	-0.07	0.17	0.09	0.04	-0.04	0.01	1.00	0.18	0.15	0.00	-0.11
$F_{HT}(t_0)$	-0.02	0.05	-0.03	0.07	-0.03	0.05	-0.03	-0.10	-0.01	-0.01	0.01	-0.29	0.01	-0.27	-0.12	-0.06	-0.16	0.00	-0.11	-0.02	0.01	0.18	1.00	0.05	0.05	-0.04
θ_{LT}	0.02	-0.01	-0.05	0.01	0.00	0.04	0.10	0.09	-0.15	-0.06	-0.04	-0.10	0.10	0.04	-0.01	-0.05	-0.11	0.03	-0.01	0.01	0.05	0.15	0.05	1.00	0.01	-0.07
θ_{MT}	0.03	0.07	0.03	0.13	0.08	-0.07	-0.10	0.03	-0.07	0.03	-0.02	-0.03	0.04	-0.02	0.07	0.05	-0.05	0.05	0.00	-0.06	0.05	0.00	0.05	0.01	1.00	-0.03
θ_{HT}	-0.09	-0.02	0.00	-0.04	0.08	0.01	-0.09	-0.05	0.04	-0.04	-0.12	0.09	0.04	-0.03	0.01	-0.04	0.04	-0.02	-0.13	0.02	0.03	-0.11	-0.04	-0.07	-0.03	1.00

Table S7. The correlation matrix of independent variables in crustal growth, thermal evolution, and seawater $\delta^{18}O$ models, for the initial condition of seawater $\delta^{18}O$ is 0‰ at 3.5 Ga (e.g., Muehlenbachs et al., 2003).

	f_{rw}	κ_r	κ_g	R_s	R_p	t_s	$H_{BSE}(t_p)$	$H_{CC}(t_p)$	$Q_{total}(t_p)$	$Q_c(t_p)$	ΔQ_c	f_{rev}	r	α_w	α_{LT}	α_{rev}	α_{HT}	$\phi_w(t_0)$	$\phi_{LT}(t_0)$	$\phi_{HT}(t_0)$	$\phi_f(t_0)$	n	$F_{HT}(t_0)$	θ_{LT}	θ_{MT}	θ_{HT}
f_{rw}	1.00	0.18	0.01	0.09	-0.29	-0.05	0.02	-0.11	0.03	-0.04	-0.05	0.01	0.11	-0.03	0.00	-0.02	0.00	-0.13	-0.17	0.05	0.01	-0.05	0.09	0.03	0.06	0.00
κ_r	0.18	1.00	-0.06	0.74	0.30	-0.01	-0.10	-0.02	0.04	-0.15	-0.03	0.12	-0.16	0.28	0.13	0.03	0.11	0.08	-0.07	-0.03	0.01	0.14	-0.07	-0.02	0.04	-0.03
κ_g	0.01	-0.06	1.00	-0.06	0.09	0.00	0.04	-0.01	-0.04	-0.04	-0.07	-0.08	0.05	-0.01	-0.01	0.04	0.02	-0.09	0.00	-0.04	0.08	-0.11	0.08	-0.08	-0.02	-0.06
R_s	0.09	0.74	-0.06	1.00	0.20	-0.19	-0.08	-0.02	-0.01	-0.12	-0.03	-0.01	0.15	0.20	0.15	0.02	0.01	0.07	-0.07	-0.04	0.04	0.03	-0.06	-0.08	0.04	0.02
R_p	-0.29	0.30	0.09	0.20	1.00	0.14	0.08	0.03	0.05	-0.12	0.10	0.11	-0.49	0.19	-0.01	-0.04	0.08	0.07	0.05	-0.04	0.06	0.22	-0.12	-0.02	-0.05	0.06
t_s	-0.05	-0.01	0.00	-0.19	0.14	1.00	-0.03	0.15	-0.02	0.02	-0.14	-0.01	-0.06	0.07	-0.05	-0.01	0.07	0.03	0.11	-0.04	-0.10	0.06	-0.01	-0.01	-0.04	-0.01
$H_{BSE}(t_p)$	0.02	-0.10	0.04	-0.08	0.08	-0.03	1.00	-0.01	0.26	-0.37	-0.05	0.14	-0.10	-0.08	0.03	-0.06	-0.10	-0.07	-0.01	0.01	-0.05	-0.04	-0.03	0.00	-0.04	0.02
$H_{CC}(t_p)$	-0.11	-0.02	-0.01	-0.02	0.03	0.15	-0.01	1.00	-0.15	0.16	-0.09	-0.10	0.00	0.03	0.01	0.00	0.01	0.09	0.02	-0.13	0.04	0.00	0.10	0.02	-0.12	-0.02
$Q_{total}(t_p)$	0.03	0.04	-0.04	-0.01	0.05	-0.02	0.26	-0.15	1.00	0.26	0.07	0.07	-0.09	-0.05	0.05	-0.01	0.11	-0.10	-0.05	0.05	-0.06	-0.03	-0.13	0.00	0.02	0.06
$Q_c(t_p)$	-0.04	-0.15	-0.04	-0.12	-0.12	0.02	-0.37	0.16	0.26	1.00	0.03	-0.08	0.09	0.12	0.03	-0.04	-0.13	0.02	-0.07	0.01	-0.03	0.01	0.02	-0.06	0.05	0.00
ΔQ_c	-0.05	-0.03	-0.07	-0.03	0.10	-0.14	-0.05	-0.09	0.07	0.03	1.00	0.04	0.03	0.07	-0.07	-0.04	0.07	-0.02	-0.07	0.01	0.03	0.00	-0.08	0.02	0.09	-0.07
f_{rev}	0.01	0.12	-0.08	-0.01	0.11	-0.01	0.14	-0.10	0.07	-0.08	0.04	1.00	-0.08	-0.35	-0.17	-0.09	-0.12	0.01	0.05	0.20	0.01	0.04	-0.33	0.13	0.03	0.01
r	0.11	-0.16	0.05	0.15	-0.49	-0.06	-0.10	0.00	-0.09	0.09	0.03	-0.08	1.00	-0.19	0.05	0.06	-0.03	-0.14	-0.09	0.10	-0.04	-0.32	0.05	0.00	-0.11	-0.04
α_w	-0.03	0.28	-0.01	0.20	0.19	0.07	-0.08	0.03	-0.05	0.12	0.07	-0.35	-0.19	1.00	-0.26	-0.10	0.07	0.21	-0.08	-0.04	0.12	0.03	-0.25	-0.10	-0.01	0.03
α_{LT}	0.00	0.13	-0.01	0.15	-0.01	-0.05	0.03	0.01	0.05	0.03	-0.07	-0.17	0.05	-0.26	1.00	0.00	0.09	-0.08	-0.02	-0.07	-0.10	-0.12	-0.14	-0.09	0.10	-0.06
α_{rev}	-0.02	0.03	0.04	0.02	-0.04	-0.01	-0.06	0.00	-0.01	-0.04	-0.04	-0.09	0.06	-0.10	0.00	1.00	0.13	0.00	-0.09	0.05	-0.04	0.02	-0.06	0.01	-0.14	-0.06
α_{HT}	0.00	0.11	0.02	0.01	0.08	0.07	-0.10	0.01	0.11	-0.13	0.07	-0.12	-0.03	0.07	0.09	0.13	1.00	-0.04	-0.07	0.04	-0.01	0.11	-0.25	0.10	0.08	0.02
$\phi_w(t_0)$	-0.13	0.08	-0.09	0.07	0.07	0.03	-0.07	0.09	-0.10	0.02	-0.02	0.01	-0.14	0.21	-0.08	0.00	-0.04	1.00	0.08	-0.02	0.14	0.14	-0.03	-0.12	-0.02	-0.08
$\phi_{LT}(t_0)$	-0.17	-0.07	0.00	-0.07	0.05	0.11	-0.01	0.02	-0.05	-0.07	-0.07	0.05	-0.09	-0.08	-0.02	-0.09	-0.07	0.08	1.00	-0.10	0.01	0.00	0.01	-0.02	0.02	0.07
$\phi_{HT}(t_0)$	0.05	-0.03	-0.04	-0.04	-0.04	-0.04	0.01	-0.13	0.05	0.01	0.01	0.20	0.10	-0.04	-0.07	0.05	0.04	-0.02	-0.10	1.00	0.01	-0.07	-0.09	0.09	0.09	-0.01
$\phi_f(t_0)$	0.01	0.01	0.08	0.04	0.06	-0.10	-0.05	0.04	-0.06	-0.03	0.03	0.01	-0.04	0.12	-0.10	-0.04	-0.01	0.14	0.01	0.01	1.00	0.15	-0.03	-0.07	0.10	0.05
n	-0.05	0.14	-0.11	0.03	0.22	0.06	-0.04	0.00	-0.03	0.01	0.00	0.04	-0.32	0.03	-0.12	0.02	0.11	0.14	0.00	-0.07	0.15	1.00	0.07	0.08	0.05	0.06
$F_{HT}(t_0)$	0.09	-0.07	0.08	-0.06	-0.12	-0.01	-0.03	0.10	-0.13	0.02	-0.08	-0.33	0.05	-0.25	-0.14	-0.06	-0.25	-0.03	0.01	-0.09	-0.03	0.07	1.00	-0.05	-0.01	-0.01
θ_{LT}	0.03	-0.02	-0.08	-0.08	-0.02	-0.01	0.00	0.02	0.00	-0.06	0.02	0.13	0.00	-0.10	-0.09	0.01	0.10	-0.12	-0.02	0.09	-0.07	0.08	-0.05	1.00	-0.01	-0.04
θ_{MT}	0.06	0.04	-0.02	0.04	-0.05	-0.04	-0.04	-0.12	0.02	0.05	0.09	0.03	-0.11	-0.01	0.10	-0.14	0.08	-0.02	0.02	0.09	0.10	0.05	-0.01	-0.01	1.00	-0.03
θ_{HT}	0.00	-0.03	-0.06	0.02	0.06	-0.01	0.02	-0.02	0.06	0.00	-0.07	0.01	-0.04	0.03	-0.06	-0.06	0.02	-0.08	0.07	-0.01	0.05	0.06	-0.01	-0.04	-0.03	1.00

Table S8. The correlation matrix of independent variables in crustal growth, thermal evolution, and seawater $\delta^{18}O$ models, for the initial condition of seawater $\delta^{18}O$ is -13.3‰ at 3.5 Ga (Jaffrés et al., 2007).

	f_{rw}	κ_r	κ_g	R_s	R_p	t_s	$H_{BSE}(t_p)$	$H_{CC}(t_p)$	$Q_{total}(t_p)$	$Q_c(t_p)$	ΔQ_c	f_{rev}	r	α_w	α_{LT}	α_{rev}	α_{HT}	$\phi_w(t_0)$	$\phi_{LT}(t_0)$	$\phi_{HT}(t_0)$	$\phi_f(t_0)$	n	$F_{HT}(t_0)$	θ_{LT}	θ_{MT}	θ_{HT}
f_{rw}	1.00	-0.01	-0.03	-0.10	-0.35	-0.02	-0.02	-0.05	0.07	0.07	0.06	0.05	0.00	0.01	-0.02	-0.04	0.01	0.02	-0.13	0.07	0.08	0.10	-0.03	-0.08	-0.02	0.02
κ_r	-0.01	1.00	0.07	0.79	0.30	0.13	-0.13	-0.08	0.00	-0.14	-0.07	0.25	-0.20	0.17	0.15	-0.03	0.04	-0.16	0.00	-0.02	-0.02	0.19	-0.11	-0.04	-0.05	0.03
κ_g	-0.03	0.07	1.00	0.12	0.23	-0.02	0.03	0.00	-0.12	0.07	-0.04	0.10	0.00	-0.02	0.05	-0.01	-0.08	-0.12	0.12	0.00	0.05	-0.03	0.02	0.02	-0.02	0.09
R_s	-0.10	0.79	0.12	1.00	0.35	-0.08	-0.14	-0.04	-0.08	-0.14	-0.07	0.10	0.00	0.12	0.20	-0.08	-0.07	-0.16	-0.01	-0.01	-0.10	0.13	-0.16	-0.03	0.00	0.05
R_p	-0.35	0.30	0.23	0.35	1.00	0.01	-0.01	-0.03	0.00	-0.11	-0.11	0.12	-0.31	0.10	0.06	-0.17	0.20	0.08	-0.07	-0.01	0.03	0.21	-0.10	0.03	-0.04	0.07
t_s	-0.02	0.13	-0.02	-0.08	0.01	1.00	-0.01	-0.04	0.07	0.02	0.01	0.07	-0.07	0.00	-0.12	0.11	0.03	0.06	-0.11	0.04	0.13	0.12	0.04	-0.10	0.00	-0.12
$H_{BSE}(t_p)$	-0.02	-0.13	0.03	-0.14	-0.01	-0.01	1.00	-0.06	0.21	-0.44	-0.09	0.12	0.00	-0.21	0.12	-0.26	0.05	-0.03	-0.09	-0.01	0.05	0.12	-0.03	-0.03	-0.12	-0.02
$H_{CC}(t_p)$	-0.05	-0.08	0.00	-0.04	-0.03	-0.04	-0.06	1.00	-0.24	0.12	0.06	-0.05	0.05	0.05	0.05	0.07	-0.01	0.11	-0.07	0.03	-0.04	-0.20	0.05	-0.04	-0.11	0.13
$Q_{total}(t_p)$	0.07	0.00	-0.12	-0.08	0.00	0.07	0.21	-0.24	1.00	0.24	0.01	-0.04	-0.05	-0.03	0.02	-0.02	0.10	0.06	0.11	-0.02	0.16	0.08	0.06	0.12	0.09	-0.04
$Q_c(t_p)$	0.07	-0.14	0.07	-0.14	-0.11	0.02	-0.44	0.12	0.24	1.00	0.05	-0.13	0.06	0.22	0.13	0.19	-0.23	0.02	0.02	-0.03	0.07	-0.20	0.01	0.12	0.04	0.01
ΔQ_c	0.06	-0.07	-0.04	-0.07	-0.11	0.01	-0.09	0.06	0.01	0.05	1.00	-0.02	0.10	-0.01	0.04	0.00	0.07	-0.02	0.13	-0.12	-0.01	0.02	-0.13	-0.10	-0.03	0.07
f_{rev}	0.05	0.25	0.10	0.10	0.12	0.07	0.12	-0.05	-0.04	-0.13	-0.02	1.00	0.02	-0.32	-0.24	-0.11	-0.07	-0.13	-0.08	-0.04	0.00	0.15	-0.23	-0.14	-0.08	0.04
r	0.00	-0.20	0.00	0.00	-0.31	-0.07	0.00	0.05	-0.05	0.06	0.10	0.02	1.00	-0.20	0.01	0.05	-0.14	-0.05	-0.01	0.02	0.04	-0.31	0.02	-0.09	0.06	0.00
α_w	0.01	0.17	-0.02	0.12	0.10	0.00	-0.21	0.05	-0.03	0.22	-0.01	-0.32	-0.20	1.00	-0.22	0.01	-0.01	0.07	-0.01	0.03	0.06	-0.14	-0.27	0.21	-0.02	-0.01
α_{LT}	-0.02	0.15	0.05	0.20	0.06	-0.12	0.12	0.05	0.02	0.13	0.04	-0.24	0.01	-0.22	1.00	-0.10	-0.04	0.05	0.00	0.02	0.05	-0.15	-0.13	0.09	0.10	0.04
α_{rev}	-0.04	-0.03	-0.01	-0.08	-0.17	0.11	-0.26	0.07	-0.02	0.19	0.00	-0.11	0.05	0.01	-0.10	1.00	-0.07	-0.08	0.04	0.04	-0.07	-0.08	0.20	0.07	0.03	0.00
α_{HT}	0.01	0.04	-0.08	-0.07	0.20	0.03	0.05	-0.01	0.10	-0.23	0.07	-0.07	-0.14	-0.01	-0.04	-0.07	1.00	0.03	0.05	0.13	0.08	0.22	-0.20	-0.01	-0.01	0.14
$\phi_w(t_0)$	0.02	-0.16	-0.12	-0.16	0.08	0.06	-0.03	0.11	0.06	0.02	-0.02	-0.13	-0.05	0.07	0.05	-0.08	0.03	1.00	0.09	0.01	0.03	-0.05	0.00	0.03	0.06	0.03
$\phi_{LT}(t_0)$	-0.13	0.00	0.12	-0.01	-0.07	-0.11	-0.09	-0.07	0.11	0.02	0.13	-0.08	-0.01	-0.01	0.00	0.04	0.05	0.09	1.00	0.00	0.10	0.02	0.10	0.00	-0.06	0.02
$\phi_{HT}(t_0)$	0.07	-0.02	0.00	-0.01	-0.01	0.04	-0.01	0.03	-0.02	-0.03	-0.12	-0.04	0.02	0.03	0.02	0.04	0.13	0.01	0.00	1.00	0.10	-0.04	-0.02	0.17	-0.06	-0.06
$\phi_f(t_0)$	0.08	-0.02	0.05	-0.10	0.03	0.13	0.05	-0.04	0.16	0.07	-0.01	0.00	0.04	0.06	0.05	-0.07	0.08	0.03	0.10	0.10	1.00	-0.01	0.09	-0.04	0.05	-0.03
n	0.10	0.19	-0.03	0.13	0.21	0.12	0.12	-0.20	0.08	-0.20	0.02	0.15	-0.31	-0.14	-0.15	-0.08	0.22	-0.05	0.02	-0.04	-0.01	1.00	-0.09	-0.03	-0.03	0.13
$F_{HT}(t_0)$	-0.03	-0.11	0.02	-0.16	-0.10	0.04	-0.03	0.05	0.06	0.01	-0.13	-0.23	0.02	-0.27	-0.13	0.20	-0.20	0.00	0.10	-0.02	0.09	-0.09	1.00	-0.07	-0.01	-0.03
θ_{LT}	-0.08	-0.04	0.02	-0.03	0.03	-0.10	-0.03	-0.04	0.12	0.12	-0.10	-0.14	-0.09	0.21	0.09	0.07	-0.01	0.03	0.00	0.17	-0.04	-0.03	-0.07	1.00	0.08	-0.06
θ_{MT}	-0.02	-0.05	-0.02	0.00	-0.04	0.00	-0.12	-0.11	0.09	0.04	-0.03	-0.08	0.06	-0.02	0.10	0.03	-0.01	0.06	-0.06	-0.06	0.05	-0.03	-0.01	0.08	1.00	-0.04
θ_{HT}	0.02	0.03	0.09	0.05	0.07	-0.12	-0.02	0.13	-0.04	0.01	0.07	0.04	0.00	-0.01	0.04	0.00	0.14	0.03	0.02	-0.06	-0.03	0.13	-0.03	-0.06	-0.04	1.00

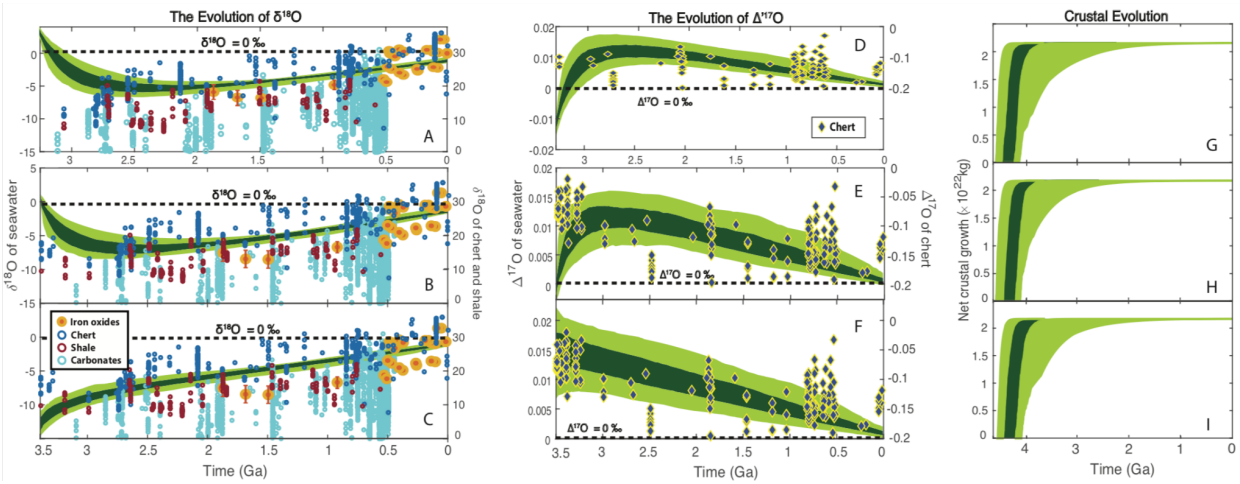

Fig. S1. The simulated Monte Carlo solutions of the seawater $\delta^{18}O$ and $\Delta'^{17}O$ evolutions, with ϕ_{si} equals 2.037 x 10^{-3}. The evolution of seawater $\delta^{18}O$ and the corresponding $\Delta'^{17}O$ and crustal evolution for the initial conditions of (A, D, G) +3.3‰ (Johnson and Wing, 2020), (B, E, H) 0‰ (e.g., Muehlenbachs et al., 2003), and (C, F, I) -13.3‰ (Jaffrés et al., 2007), respectively. The middle 50% and 90% of successful solutions are shown in dark green and light green, respectively. The iron oxide records (Galili et al., 2019) are shown in orange circles; carbonates (Prokoph et al., 2008 and references therein) are shown in light blue circles; chert and shale (Zahkarov et al., 2021; Sengupta et al., 2020; Liljestrand et al., 2020; Bindeman et al., 2016; Levin et al., 2014; and references therein) are shown in dark blue and red circles. The $\delta^{18}O$ of carbonates, chert, and shale are shown for comparison but not used to select successful solutions. The corresponding evolution of seawater $\Delta'^{17}O$ for (A) to (C) are compared with chert records (Zahkarov et al., 2021; Sengupta et al., 2020; Liljestrand et al., 2020; Lowe et al., 2020; Levin et al., 2014; blue dice).

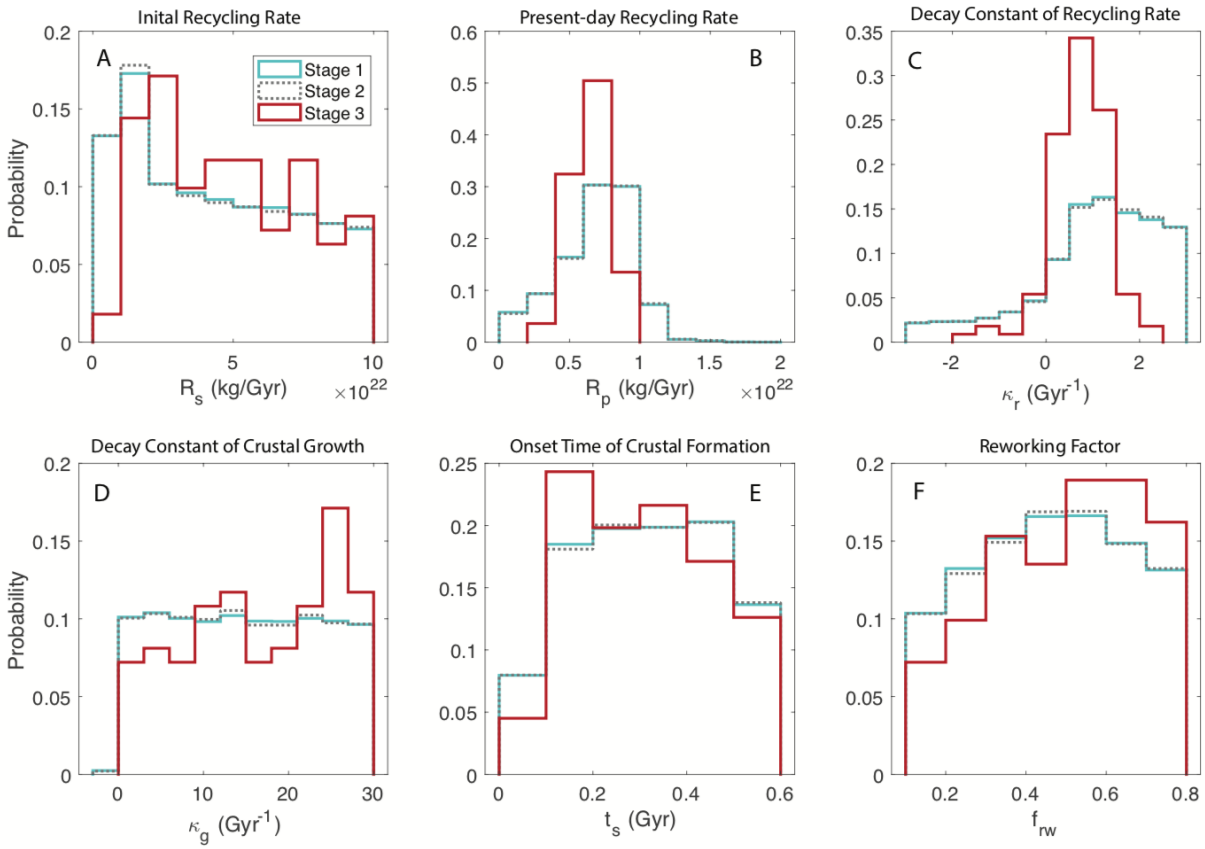

Fig. S2. The a posteriori distributions of crustal evolution parameters, based on ~2x10^4, ~2.5x10^4, and ~3x10^3 successful Monte Carlo solutions from stage 1 to 3 (for the initial conditions of seawater δ^{18}O is 0‰ at 3.5 Ga (e.g., Muehlenbachs et al., 2003)), respectively. Distributions from stage 1 to 3 are shown in blue, gray, and red, respectively. (A) Initial recycling rate, (B) present-day recycling rate, (C) decay constant for crustal recycling, (D) decay constant for crustal generation, (E) onset time for crustal formation, and (F) reworking factor.

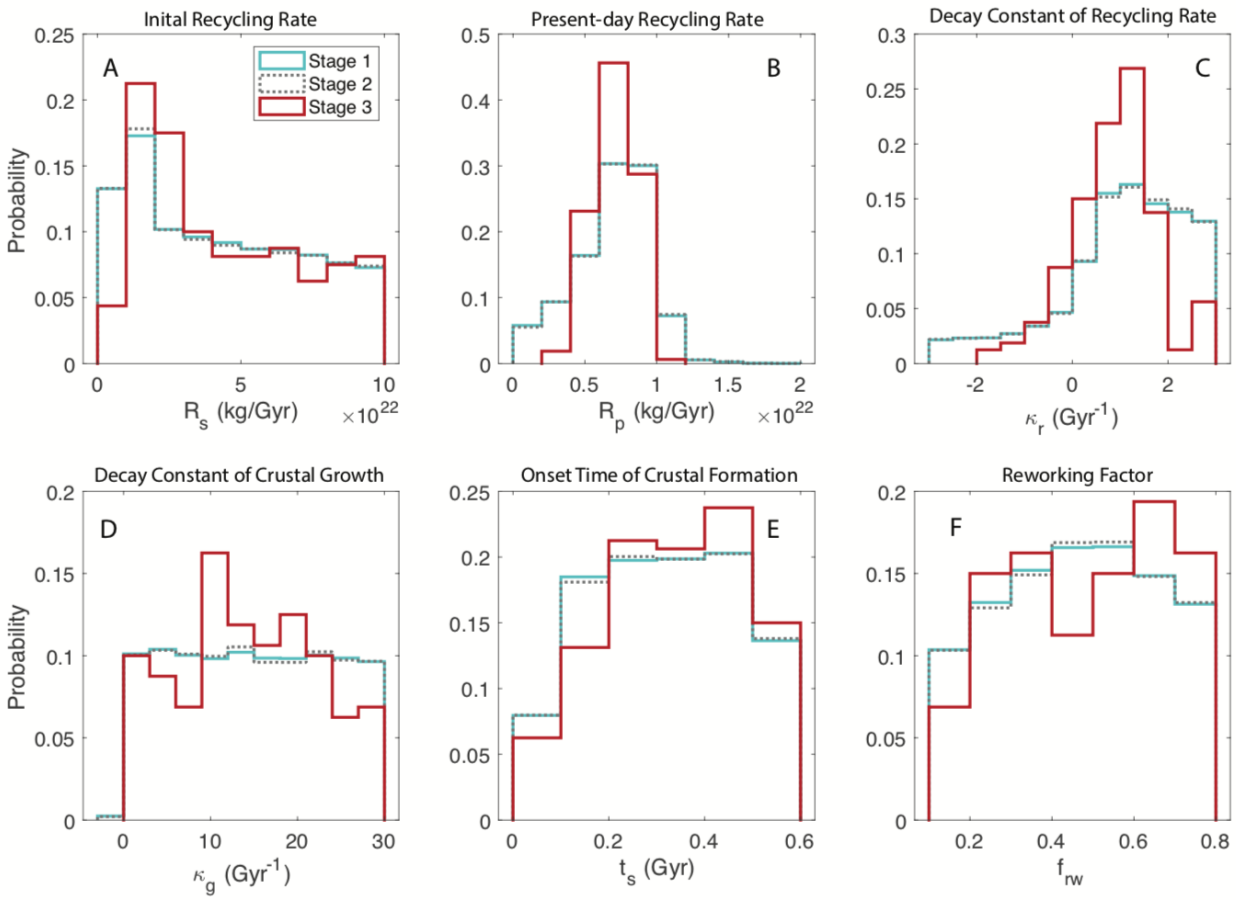

Fig. S3. The a posteriori distributions of crustal evolution parameters, based on ~2x10^4, ~2.5x10^4, and ~3x10^3 successful Monte Carlo solutions from stage 1 to 3 (for the initial conditions of seawater δ^{18}O is -13.3‰ at 3.5 Ga (Jaffrés et al., 2007)), respectively. Distributions from stage 1 to 3 are shown in blue, gray, and red, respectively. (A) Initial recycling rate, (B) present-day recycling rate, (C) decay constant for crustal recycling, (D) decay constant for crustal generation, (E) onset time for crustal formation, and (F) reworking factor.

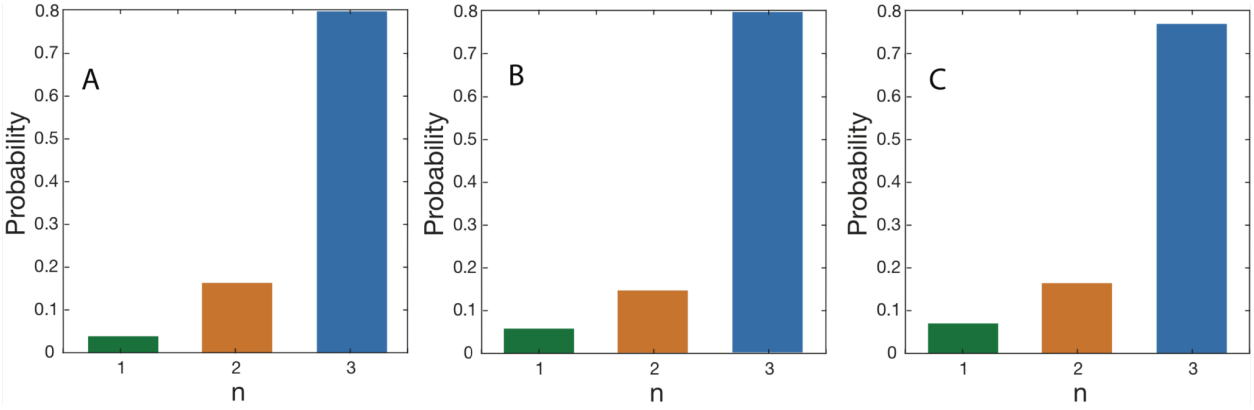

Fig. S4. The a posteriori distribution of the exponent *n* in equation (3), based on ~1 x 10^4, ~ 1.8 x 10^4, and ~3 x 10^3 successful Monte Carlo solutions for the initial conditions of seawater $\delta^{18}O$ is (A) +3.3‰ (Johnson and Wing, 2020), (B) 0‰ (e.g., Muehlenbachs et al., 2003), and (C) -13.3‰ (Jaffrés et al., 2007), respectively. When *n* equals 1 (green bars), equation (3) corresponds to a linear dependence of high-temperature alteration of oceanic crust on plate velocity, whereas *n* equals 2 (orange bars) and 3 (blue bars) represents a nonlinear dependence.

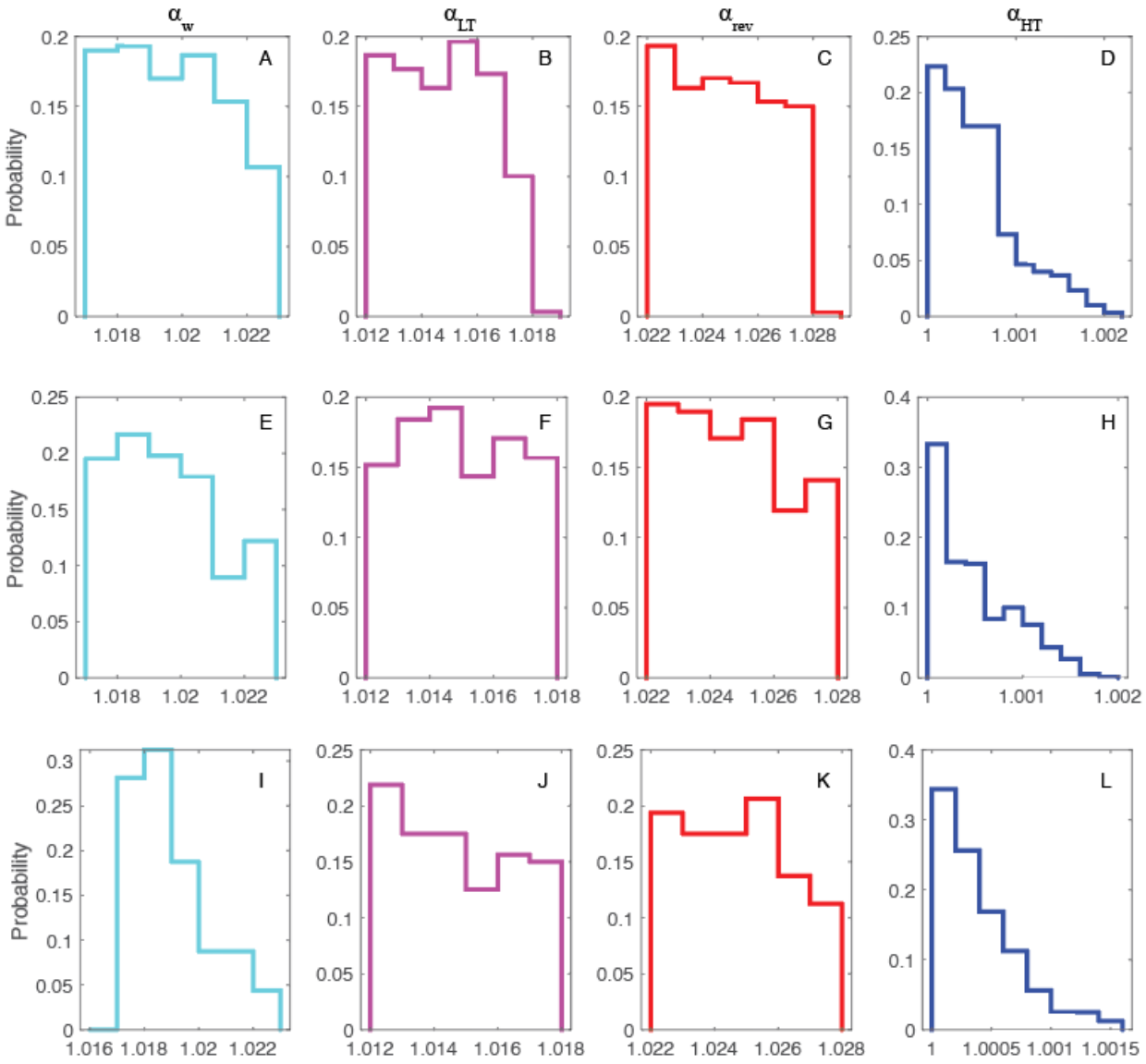

Fig. S5. The a posteriori distribution of isotope fractionation factors during Urey reaction (α_w), low-T alteration (α_{LT}), reverse weathering (α_{rev}), and high-T alteration (α_{HT}), based on ~3 x 10^3 successful Monte Carlo solutions for the initial conditions of (A-D) +3.3‰ (Johnson and Wing, 2020), (E-H) 0‰ (e.g., Muehlenbachs et al., 2003), and (I-L) -13.3‰ (Jaffrés et al., 2007), respectively.

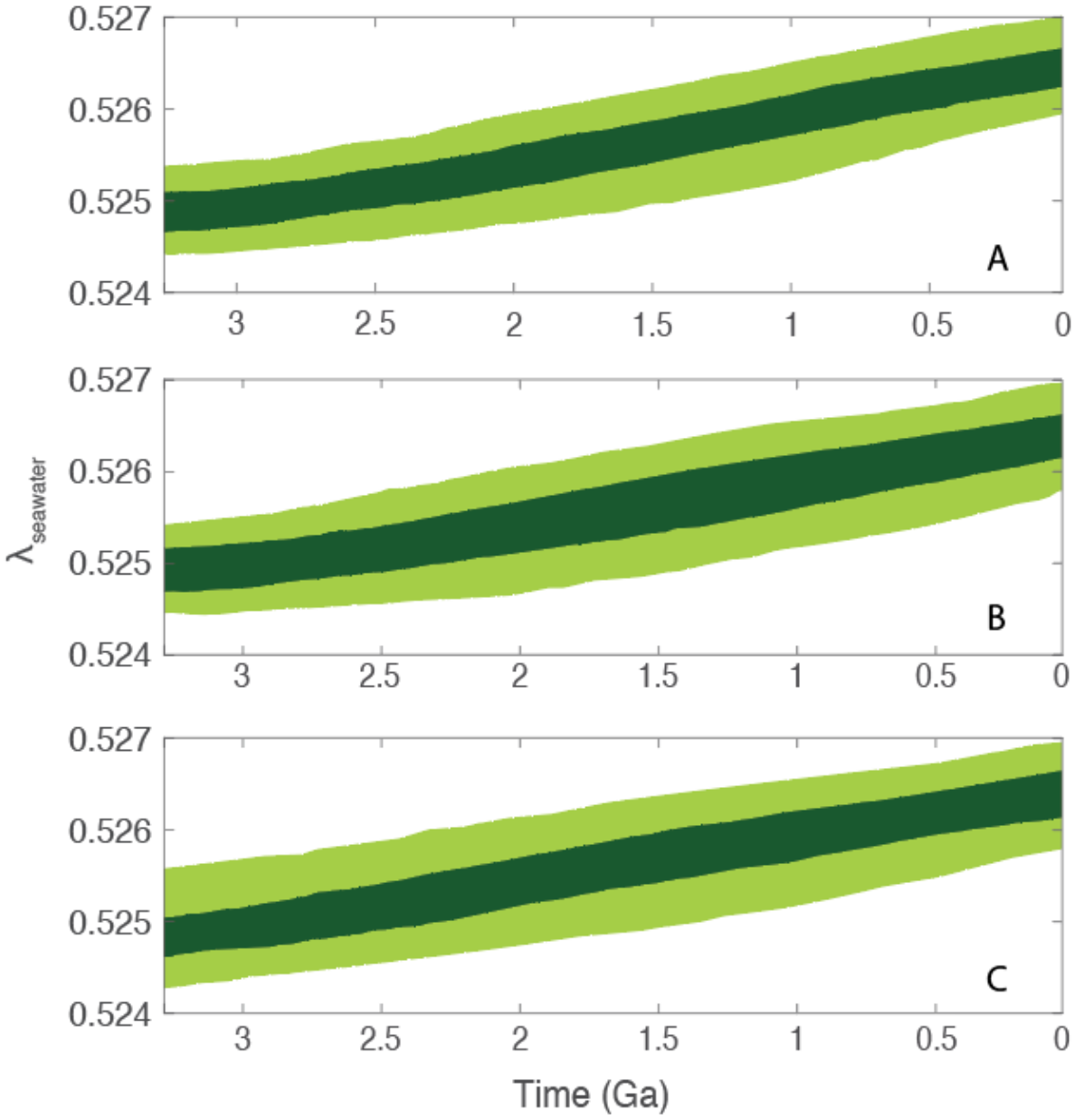

Fig. S6. The simulated Monte Carlo solutions of $\lambda_{seawater}$ (for the initial conditions of seawater $\delta^{18}O$ is (A) +3.3‰ (Johnson and Wing, 2020), (B) 0‰ (e.g., Muehlenbachs et al., 2003), and (C) -13.3‰ (Jaffrés et al., 2007), respectively. The middle 50% and 90% of successful solutions are shown in dark green and light green, respectively.

868
869
870

871 **Reference**

872 Guo, M., Korenaga, J., Argon constraints on the early growth of felsic continental crust. *Sci.*
873 *Adv.*, ***6***, eaaz6234 (2020). DOI: 10.1126/sciadv.aaz6234.
874 Wallmann, K., The geological water cycle and the evolution of marine $\delta^{18}O$ values. *Geochim.*
875 *Cosmochim. Acta*, **65**, 2469-2485 (2001). DOI: https://doi.org/10.1016/S0016-
876 7037(01)00603-2.